

1
2
3
4
5
6
7
8
9
10
11
12
13
14
15
16
17
18
19
20
21
22
23
24
25
26
27
28
29
30
31
32
33
34
35
36
37
38
39
40
41
42
43

Observations of Shoaling Internal Wave Transformation Over a Gentle Slope in the South China Sea

Steven R. Ramp¹, Yiing Jang Yang², Ching-Sang Chiu³, D. Benjamin Reeder³, and Frederick L. Bahr⁴

Last modified ~~February 1, 2022~~
Submitted to: Nonlinear Processes in Geophysics

Deleted: January
Deleted: 19

[1] {Soliton Ocean Services LLC, Falmouth, MA 02540}
[2] {Institute of Oceanography, National Taiwan University, Taipei, Taiwan}
[3] {Dept. of Oceanography, Naval Postgraduate School, Monterey, CA 93943}
[4] {Monterey Bay Aquarium Research Institute, Moss Landing, CA 95039}
Correspondence to: S. R. Ramp (sramp@solitonocean.com)

46 **Abstract**

47
48
49
50
51
52
53
54
55
56
57
58
59
60
61
62
63
64
65
66
67
68
69

Four oceanographic moorings were deployed across the South China Sea continental slope near 21.85°N, 117.71°E, from May 30 to July 18, 2014 for the purpose of observing high-frequency nonlinear internal waves (NLIWs) as they shoaled across a rough, gently sloping bottom. Individual waves required just two hours to traverse the array and could thus easily be tracked from mooring-to-mooring. In general, the amplitude of the incoming NLIWs ~~tracked~~ the fortnightly tidal envelope in the Luzon Strait, lagged by 48.5 hours, ~~but~~ were smaller than the waves ~~previously~~ observed 50 km to the southwest near the Dongsha Plateau. The type a-waves and b-waves were observed, with the b-waves always leading the a-waves by 6-8 hours. Most of the ~~NLIWs~~ were remotely generated, but a few of the b-waves formed locally via convergence and breaking at the leading edge of the upslope ~~propagating~~ internal tide. Waves incident upon the ~~moored~~ array with amplitude less than 50 m and energy less than 100 MJ m⁻¹ propagated adiabatically upslope with little change of form. Larger waves formed packets via wave dispersion. For the larger waves, the kinetic energy flux decreased sharply upslope between 342 m to 266 m while the potential energy flux increased slightly, causing an increasing ratio of potential-to-kinetic energy as the waves shoaled. The results are in rough agreement with recent theory and numerical simulations of shoaling waves.

- Deleted: was a good match with
- Deleted: and
- Deleted: now-familiar
- Deleted: waves

74 1 Introduction

75 Considerable field work has now been dedicated to observing and understanding
76 the very large amplitude, high-frequency nonlinear internal waves (NLIW) in the
77 northeastern South China Sea (SCS). It has now been well established that the
78 waves emerge from the internal tide which is generated by the flux of the barotropic
79 tide across the two ridges in the Luzon Strait [Buijsman et al., 2010a, 2010b; Zhang
80 et al., 2011]. Both tidal conversion and dissipation are high around the ridges
81 [Alford et al., 2011], but adequate energy survives to escape the ridges and
82 propagate WNW across the sea. As they do so, the internal tides steepen nonlinearly
83 until eventually the NLIW are formed [Farmer et al., 2009; Li and Farmer, 2011;
84 Alford et al., 2015]. The longitude where this takes place depends on the details of
85 the forcing and stratification but based on satellite imagery it is not until at least
86 120° 30'E, roughly 50 km west of the western (Heng-Chun) ridge [Jackson, 2009].
87 This longitude is hypothesized to be the minimum distance/time required for the
88 internal tide to nonlinearly steepen and break, or perhaps the first point where tidal
89 beams intersect the sea surface west of the western ridge. Once the NLIW have
90 formed, they propagate WNW across the deep SCS basin with remarkably little
91 change of form [Alford et al., 2010; Ramp et al., 2010]. Once the waves start to shoal
92 on the continental slope however, roughly between 1000m to 150m depth, the
93 changes become quite dramatic. Wave refraction due to the shallower depth and
94 changing stratification tends to align the wave crests with the local topography.
95 Incident NLIWs which were initially solitary may form packets via wave breaking or
96 dispersion [Vlasenko and Hutter, 2002; Vlasenko and Stashchuk, 2007; Lamb and
97 Warn-Varnas, 2015]. Some very large waves may split into two smaller waves
98 [Small 2001a, 2001b; Ramp, 2004]. When the wave's orbital velocity exceeds the
99 propagation speed, usually between 300m - 150m depth, the largest waves may
100 break and form trapped cores that transport mass and nutrients onshore [Farmer et
101 al., 2011; Lien et al., 2012, 2014; Rivera-Rosario et al., 2020; Chang et al., 2021]. Still
102 farther onshore where the upper layer thickness exceeds the lower, the depression
103 waves are transformed into elevation waves [Orr and Mignerey, 2003; Duda et al.,
104 2004; Ramp et al., 2004; Liu et al., 2004]. The elevation waves presumably continue
105 propagating WNW towards shore and dissipate in shallow water, but observations
106 to the west of this point are scarce.

107
108 Two types of NLIWs, called a-waves and b-waves, have been repeatedly observed, a
109 parlance first coined by Ramp et al. [2004]. Based on the Asian Seas International
110 Acoustics Experiment (ASIAEX) results, the a-waves consisted of rank-ordered
111 packets that arrived at the same time every day and were generally larger than the
112 b-waves, which were usually solitary and arrived one hour later each day. It has
113 subsequently been shown via longer data sets that the timing is not universal and
114 that b-waves may sometimes be larger than a-waves [Alford et al., 2010; Ramp et al.,
115 2010]. It is now recognized that the a-waves are generated in the southern portion
116 of the Luzon Strait and the b-waves to the north [Du et al., 2008; Zhang et al., 2011;
117 Ramp et al., 2019]. The b-waves are subject to massive dissipation over the shallow
118 northern portion of the western (Heng-Chun) ridge [Alford et al., 2011] but the a-

Deleted: an impressive

Deleted: are

Deleted: waves

Deleted: ; Lien et al.,

Deleted: The correct manner of classification is likely via their generating mechanism and location, but with regard to this much controversy still remains. All agree that the waves stem from the Luzon Straits, where the barotropic tide has a large fortnightly envelope, a strong diurnal variation, and is asymmetric with stronger tides on ebb (towards the Pacific) than on flood (towards the SCS). Some authors assert that both types of waves are released on flood, with a-waves formed on the strong beat and b-waves on the weak beat [Vlasenko et al., 2012]. Others find both types generated on ebb, with a-waves formed at the east ridge and b-waves at the west ridge [Chen et al., 2013]. A third school of thought finds the a-waves formed on the larger of the two ebb tides and the b-waves on the larger flood [Alford et al., 2010; Ramp et al., 2010]. Finally, both types of waves may be spawned by the same tidal beat but at different locations in the strait [Du et al., 2008; Zhang et al., 2011; Ramp et al., 2019]. A resolution is desirable not only for its intrinsic scientific worth, but also to improve the accuracy of NLIW prediction schemes presently being implemented in the SCS.

145 waves are not. The distinction matters because the energy and propagation
146 direction of the trans-basin waves incident on the continental slope determines how
147 they behave as they shoal. These differences are explored further in this paper.

Deleted:

149 The present study was motivated by the discovery of large ($h > 15\text{m}$, λ order 350m)
150 undersea sand dunes on the sea floor along a transect southeastward from 21.93°N,
151 117.53°E in the northeastern South China Sea [Reeder et al., 2011]. Subsequent
152 multi-beam echo surveys (MBES) during 2013 and 2014 revealed that the dunes
153 occupy at least the region spanning 21.8 to 21.9°N and 117.5 to 117.7°E (Figure 1).
154 This region is on the continental slope slightly northeast of the Dongsha Plateau.
155 The bottom slope in the dunes region is relatively slight with respect to steeper
156 bottom slopes progressing both offshore and onshore from the dune field. The sand
157 dunes are of interest due to their impact on shallow-water acoustic propagation,
158 and their interaction with shoaling internal tides and NLIWs traveling WNW up the
159 slope. The acoustic issues are addressed in other papers emerging from the
160 program [Chiu and Reeder, 2013; Chiu et al., 2015]. Oceanographic questions of
161 interest include: 1) How are NLIWs transformed as they shoal over a gentle slope
162 between 388m and 266m over the continental slope? 2) What are the physical
163 mechanisms responsible for this transformation? and 3) How does the increased
164 bottom roughness in the dune field affect energy dissipation in the shoaling internal
165 tides and NLIWs, relative to other locations? Geophysical problems of interest
166 include: 4) What, if any, is the role of the NLIW in sediment re-suspension and dune
167 building? 5) What determines the spatial scales of the dunes? and 6) Why are the
168 dunes located where they are, and why are they not observed elsewhere?

Deleted: 0

Deleted: there

169
170 This paper addresses how the high-frequency nonlinear internal waves were
171 transformed under shoaling, while the NLIW dissipation and role in the dune-
172 building process will be addressed in separate works [Helfrich et al., 2022]. The
173 data and methods are described in section 2, the NLIW arrival patterns and their
174 relation to the source tides in section 3, and the wave transformations and energy
175 conservation in section 4. A summary and conclusion section follows.

Deleted: ¶

Deleted: ¶
Towards this end, a pilot study was conducted during May 2013 followed by a major field experiment during June 2014 to address the questions above. An array of environmental and acoustic moorings was deployed from the R/V OCEAN RESEARCHER 1 during June 1-12 and recovered from the R/V OCEAN RESEARCHER 5 during June 15-30, 2014 (Figure 1). While the moorings were in the water, a number of CTD stations and near-bottom time series were obtained from the research vessels to study the wave/bottom interactions. A second research vessel (OCEAN RESEARCHER 3) conducted towed-source operations nearby.

176 2 Data and Methods

177
178
179 An array of four oceanographic moorings were deployed across the continental
180 slope from 21.81°N, 117.86°E (386 m) to 21.89°N, 117.56°E (266 m) during May 31
181 to June 18, 2014 (Figure 1, Table 1). The moorings labeled YPO2, YPO1, CPO, and
182 RPO were separated by 4.10, 3.30, and 5.69 km respectively corresponding to wave
183 travel times of 36.5, 30.3, and 56 min between moorings. Temperature and salinity
184 were sampled at 60s intervals. Instrument spacing ranged from 15 m to a maximum
185 of 30 m in the vertical to resolve internal wave amplitudes. Currents at RPO were
186 sampled using three downward looking 300 kHz ADCPs moored at 27 m, 105 m, and
187 184 m depth which provided coverage of the entire water column except the
188 upper 20 m. Currents at CPO were also sampled using three 300 kHz ADCPs, one
189 downward-looking unit moored at 15 m depth, and an up/down pair at 264 m

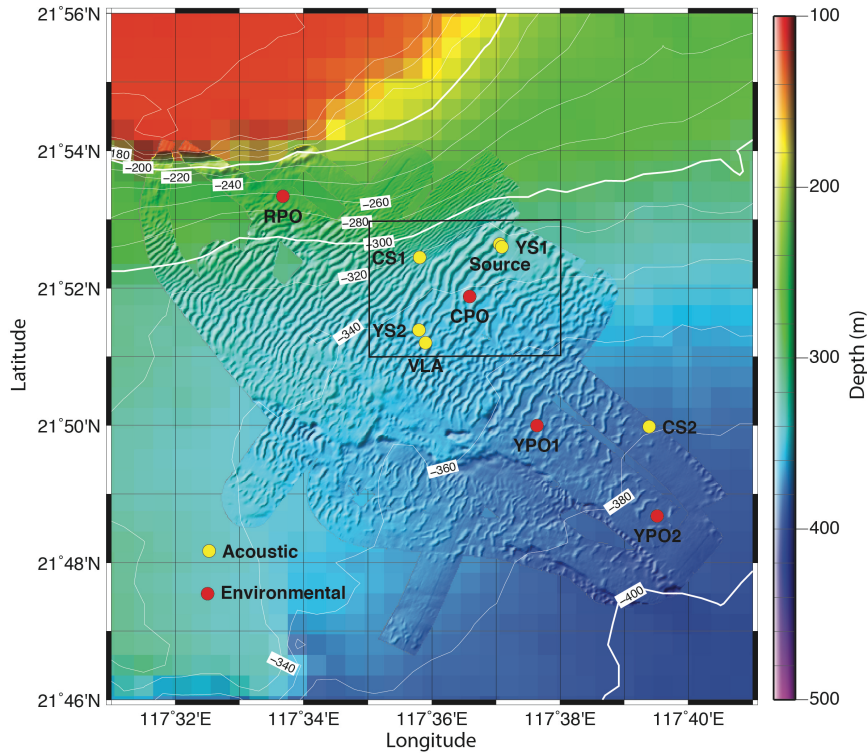
Deleted: tidal

Deleted: es

Formatted: Left, No widow/orphan control

Deleted: , such that individual waves could easily be identified and traced across the array

Deleted:



212
 213
 214 *Figure 1. Locator map for the Sand Dunes 2014 field experiment. This paper primarily*
 215 *concerns the environmental moorings indicated by the red dots, although temperature*
 216 *from the “source” mooring is also used. The area within the black box is expanded in*
 217 *Figure 2.*

219 depth. Since the range of these instruments was nominally 100 m, there was an
 220 unsampled region spanning roughly 115 – 164 m depth at mooring CPO. Currents at
 221 YPO1 and YPO2 were sampled using one 75 kHz and one 300 kHz ADCP. The 75
 222 kHz instruments were mounted downward looking in the top syntactic foam sphere
 223 at 20 m depth. The 300 kHz instruments were also mounted downward looking in
 224 cages at 300 m depth. The 300 kHz instruments burst-sampled for 20 s every 90 s,
 225 while the 75 kHz instruments sampled once per second and were averaged to 90 s
 226 intervals during post-processing. These sampling rates were adequate to observe
 227 the shoaling NLIWs with no aliasing. A fifth mooring labeled “source” on roughly
 228 the same isobath as CPO (Figure 1) sampled temperature only from 27 to 267 m.
 229 This mooring was targeted for the same “trough” in the sand dune field as CPO to

230 examine along-crest acoustic propagation. It additionally proved useful to identify
231 the precise phasing and orientation of the internal wave crests in the along-slope
232 direction.

233

234 3 Results

235

236 3.1 The Nature of the Dunes

237

238 The stage is set by a zoomed-in view of the study region showing the seafloor sand
239 dunes as depicted by the MBES data (Figure 2). A change in the bottom slope forms
240 a very clear line of demarcation between lower (4 m) dunes with shorter (100 m)
241 wavelength and the larger (10-15 m) dunes with longer (260 m) wavelength. Dunes
242 in these regions were nearly sinusoidal. Farther down the slope in water > 360m
243 depth, the dunes were “parted” meaning the trough widths were much greater than
244 the crest widths. Mooring RPO was located in the first region with steeper slope,
245 CPO was in the second region of smaller slope and large sinusoidal dunes, and
246 moorings YPO1 and YPO2 were in a region with similar mean bottom slope but
247 parted dunes. Repeat MBES surveys indicated that during 2013-14, the dunes were
248 stationary to within the accuracy of the surveys. For purposes of this paper, the
249 most important fact about the bottom is the sharp, clear change of bottom slope
250 across the white dotted line (Figure 2) from 1:35 = .03 = 3% = 2.0° over the
251 shallower part to 1:160 = .006 = 0.6% = 0.3° over the deeper part. These slopes are
252 essential for comparing the observations to theory.

253

254

255

256 3.2 Wave Arrival Patterns

257

258 While fine-tuning the NLIW generation problem is beyond the scope of this paper, the
259 fundamental properties of the wave arrival patterns can be understood via comparisons
260 with the generating tide in the Luzon Strait. Having no remote observations during
261 spring 2014, the wave arrival patterns at the sand dunes moored array were compared
262 with the barotropic tidal forcing in the Luzon Strait as obtained from the TPXO7.0 global
263 tidal model [Egbert and Erofeeva, 2002]. The model output has been shown to be in
264 good agreement with the limited observations available in the Luzon Strait [Ramp et al.,
265 2010] and is thus a good indication of the tidal amplitude and phase at generation.

266

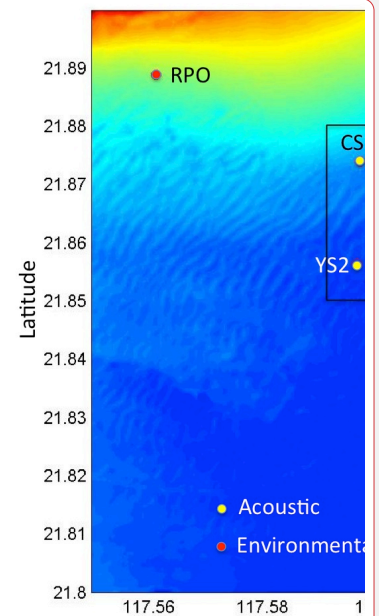
267 To begin, all the NLIWs arriving at the moored array were identified using large-scale
268 plots of temperature, salinity, and velocity. The arrivals were then summarized for the
269 entire time series by labeling the displacement of the 20°C isotherm from its mean
270 position at mooring RPO (Figure 3, top). The wave arrivals, as indicated by sharp
271 downward displacements of the isotherm, fall into two groups or “clusters” of waves each
272 within a fortnightly envelope. The waves were labeled using previous conventions, using
273 lowercase a- and b- for the first cluster and uppercase A- and B- for the second for
274 uniqueness. This nomenclature will be used to refer to individual waves subsequently.
275

Deleted: ¶

Continuous underway sampling of velocity and backscatter was achieved using the ships' hull mounted ADCPs and echo sounders. These were a narrow-band 150 kHz ADCP system and EK500 on the OR1 and a 75 kHz Ocean Surveyor with fish finder on the OR5. The ship's radar images, which clearly showed the surface expression of the NLIWs, were recorded once per minute throughout the cruises. MODIS ocean color imagery for the region was collected and archived when available. ¶

Moved (insertion) [1]

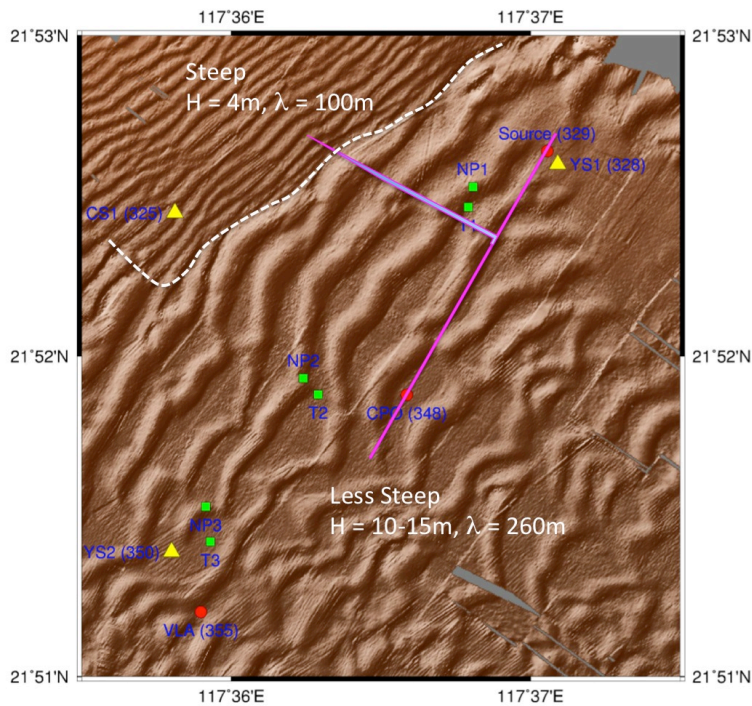
Deleted: . Bottom sediment grabs revealed that the dunes were composed of sand and gravely sand near the crests, and finer clayey and silty sand in the troughs. More details on the sediment characteristics may be found in a subsequent paper on dune formation.



Deleted:

¶ Figure 1. Locator map for the Sand Dunes 2014 field experiment. This paper primarily concerns the environmental moorings indicated by the red dots, although temperature from the “source” mooring is also used. The mean bottom depth ranged from 388 m at YPO2 to 266 m at RPO. The sand dunes on the sea floor look like ripples in this image. The area within the black box is expanded in Figure 2. ¶

Moved (insertion) [2]



302
303
304
305
306
307
308
309
310
311
312
313
314
315
316
317
318
319
320
321
322

Figure 2. The sea floor in the study region as observed by a multi-beam echo sounder (MBES) survey during June 2014. The region is delineated by the black box in Figure 1. The dotted white line indicates a sharp change in bottom slope, steeper towards the northwest. The magenta arrow indicates the direction of propagation of the nonlinear internal waves (NLIW) as determined by wave arrival times at moorings CPO and "source," (pink line).

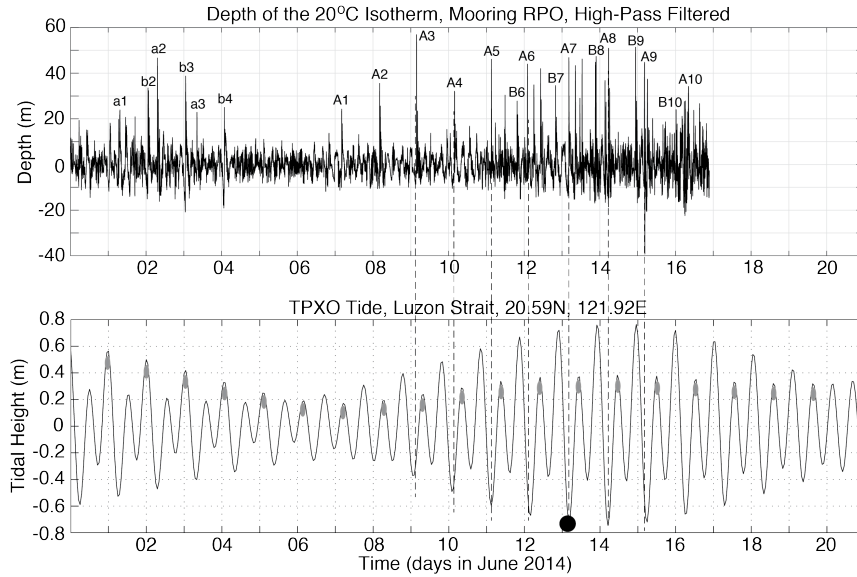
There is no dynamical difference between the two. A total of 21 NLIWs with amplitude greater than 20 m were observed, 13 a-waves and 8 b-waves. When b-waves were present, the waves arrived in b- and a- pairs with the b-wave always leading the a-wave by on average 6.6 hours. The a-waves began arriving earlier in the fortnightly cycle for instance 6/7 to 6/11. The b-waves began arriving later and grew larger later in the fortnightly cycle. With the exception of 6/3 and 6/15, the a-waves were larger than the b-waves.

The RPO wave amplitude time series was then plotted over the Luzon Strait tides (Figure 3, bottom) with the wave amplitudes lagged back by the propagation time from the source to the mooring. The lag time (48.5 hours) was estimated by making a small

Deleted: temperature sensors on
Deleted: .

Formatted: No widow/orphan control

§25



§26

§27

§28

§29

§30

§31

§32

§33

§34

§35

§36

§37

§38

§39

§40

§41

§42

§43

§44

§45

§46

§47

§48

§49

§50

Figure 3. (Top) Time series showing the depth of the 20°C isotherm observed by mooring RPO located at the 266 m isobath (Figure 1). The time series was high pass filtered to separate thermal displacements due to NLIWs from the internal tides and mean (mesoscale and seasonal) flows. The sharp depressions of the isotherm indicate passing NLIWs. The type-a and type-b waves are labeled using lower case for the first fortnight and upper case for the second. (Bottom) Tidal amplitude in the central Luzon Strait from the TPXO global tidal model [Egbert and Erofeeva, 2002], at a point located between Batan and Itbayat Island in the Luzon Strait. The gray ellipses indicate how the major and minor tidal beats switched positions during the neap tide. The black circle indicates the time of the full moon on June 13th. The waves (top panel) have been lagged back by the propagation time from the strait (48.5 hours) to better align with the barotropic tidal envelope in the generating region. The vertical dashed lines show how the lagged a-waves aligned with the ebb tide in the straits.

Formatted: Superscript

adjustment to the propagation time nearby (50.3 hours) which was calculated using a full year's data [Ramp et al., 2010]. Several obvious results emerge from this comparison. First, the NLIW amplitudes at RPO track the fortnightly tidal amplitudes in the Luzon Strait. The largest waves were generated at spring tide in the strait and no waves at all were generated during neap. Second, the generating tide was mixed, diurnal dominant, with a strong diurnal variation, but only the major beats resulted in NLIWs in the far field. The minor beats and the neap tides were apparently too weak to spawn NLIWs

§51 downstream. As a result, just on wave type of each type was generated per day, despite
§52 the generating tide being semidiurnal. The major and minor beats switched positions
§53 during the neap tide, and the wave arrivals at the sand dunes array switched positions
§54 accordingly. Third, the lagged a-waves aligned precisely with the major ebb (eastward)
§55 tide in the Luzon Strait, in agreement with previous work. This suggests generation by
§56 the lee wave mechanism [Buijsman et al., 2010a]. Finally, the b-waves were sometimes
§57 aligned well with the major flood tide preceding each a-wave, but we now believe this to
§58 be coincidence: The directional histograms (not shown) show the a-waves on average
§59 traveling along a path about 24 degrees more northward (294°) than the b-waves (270°),
§60 consistent with the primary source for the a-waves being located farther to the south
§61 along the Luzon ridge system. The b-waves lead because their generation site was closer
§62 to our observation point on the Chinese continental slope.

§64 One example of the daily moored temperature time series at mooring RPO is shown to
§65 further illustrate these results (Figure 4). During June 9 to 13, the A-waves arrived at
§66 about the same time each day while from June 14-18, they arrived about an hour later
§67 each day. This result, that the A-wave arrival times were constant early in the fortnightly
§68 tidal cycle but delayed an hour per day as the waves increased in amplitude later in the
§69 cycle was consistent with the model results of [Chen et al., 2013]. Wave A7 on June 15
§70 was anomalously late by about 2 hours relative to waves A6 and A8. This is attributed
§71 to the passing of tropical storm Hagabus on June 14-15 with accompanying strong wind-
§72 forced currents. The B-wave arrivals began at about 20:00 on June 13, and were
§73 subsequently delayed about an hour per day, similar to the corresponding A-waves
§74 (Figure 4). The difference in the arrival times between the B-waves and the A-waves was
§75 6:30, 8:25, 6:15, and 5:50 on June 14-17 respectively. On June 16-18 two A-waves of
§76 near equal amplitude arrived about 2 hours apart. These “double A-waves” appeared
§77 over the slope only near spring tide in the Luzon Straits, and the second one has been
§78 designated by a prime. The origin of these waves is unclear. We speculate that the new
§79 A' waves originated from a different (third) source in the Luzon Straits that is only active
§80 under maximum barotropic forcing. More observations in the source region are needed
§81 to understand the wave generation issues, including this double a-wave phenomenon.

§84 3.3 Wave Transformation Over the Slope

§86 Many significant wave transformations were observed between the 386 m (YPO2)
§87 and the 266 m (RPO) isobaths over the upper continental slope. Three sections of
§88 the record are shown to illustrate different phenomena. The first sequence from
§89 June 2 to 6 evolved out of moderate and decreasing forcing in the Luzon Strait
§90 (Figure 3). The observations captured the local steepening and breaking of the tidal
§91 front to form b-waves as it shoaled (Figure 5). The internal tides at YPO2 were
§92 diurnal and nearly sinusoidal with an amplitude of about 4°C (blue line). The a-
§93 waves were already evident at YPO2, but not the b-waves. Then, beginning at YPO1
§94 and continuing to CPO, the leading edge of the tidal front became very steep with a
§95 temperature change of 1°C / min for 5 minutes at CPO (black ellipses in Figure 5).
§96 This front subsequently broke and formed b-wave packets b2 and b3 observed at

Moved up [1]: wavelength and the larger (10-15 m) (260 m) wavelength. Dunes in these regions were nearly sinusoidal. Farther down the slope in water > 360m depth, the dunes were “parted” meaning the trough widths were much greater than the crest widths. Mooring RPO was located in the first region with steeper slope, CPO was in the second region of smaller slope and large sinusoidal dunes, and moorings YPO1 and YPO2 were in a region with similar mean bottom slope but parted dunes. Repeat MBES surveys indicated that during 2013-14, the dunes were stationary. Bottom sediment grabs revealed that the dunes were composed of sand and gravelly sand near the crests, and finer clayey and silty sand in the troughs. More details on the sediment characteristics may be found in a subsequent paper on dune formation. For purposes of this paper, the most important fact about the bottom is the sharp, clear change of bottom slope across the white dotted line (Figure 2) from 1:35 = .03 = 3% = 2.0° over the shallower part to 1:160 = .006 = 0.6% = 0.3° over the deeper part. These slopes are essential for comparing the observations to theory. ¶

Deleted: Understanding the wave arrival patterns during the experiment requires understanding the barotropic tidal forcing in the Luzon Strait. Since no observations were available from the strait, the tidal beat was obtained from the TPX07.0 global tidal model [Egbert and Erofeeva, 2002]. The tidal heights have been shown to be in good agreement with the limited observations available in the Luzon Strait [Ramp et al., 2010] and are thus a good indication of the tidal phase at generation. Since the tide in the SCS is a progressive wave moving east to west, high tide corresponds to westward current and low tide to eastward current... [1]

Moved (insertion) [3]

Moved up [2]: 3.2 Wave Arrival Patterns ¶

¶ Understanding the wave arrival patterns during the experiment requires understanding the barotropic tidal forcing in the Luzon Strait. Since no observations were available from the strait, the tidal beat was obtained from the TPX07.0 global tidal model [Egbert and Erofeeva,

Moved (insertion) [4]

Moved up [3]: The lagged a- and b-wave arrival times from mooring RPO lined up precisely with the major ebb and flood tidal peaks respectively. (Note that the minor tidal peaks in the Luzon Strait never produced a downstream NLIW at any time.) Each wave arrival has been identified and labeled using a nomenclature which will be maintained throughout the paper. The arrivals

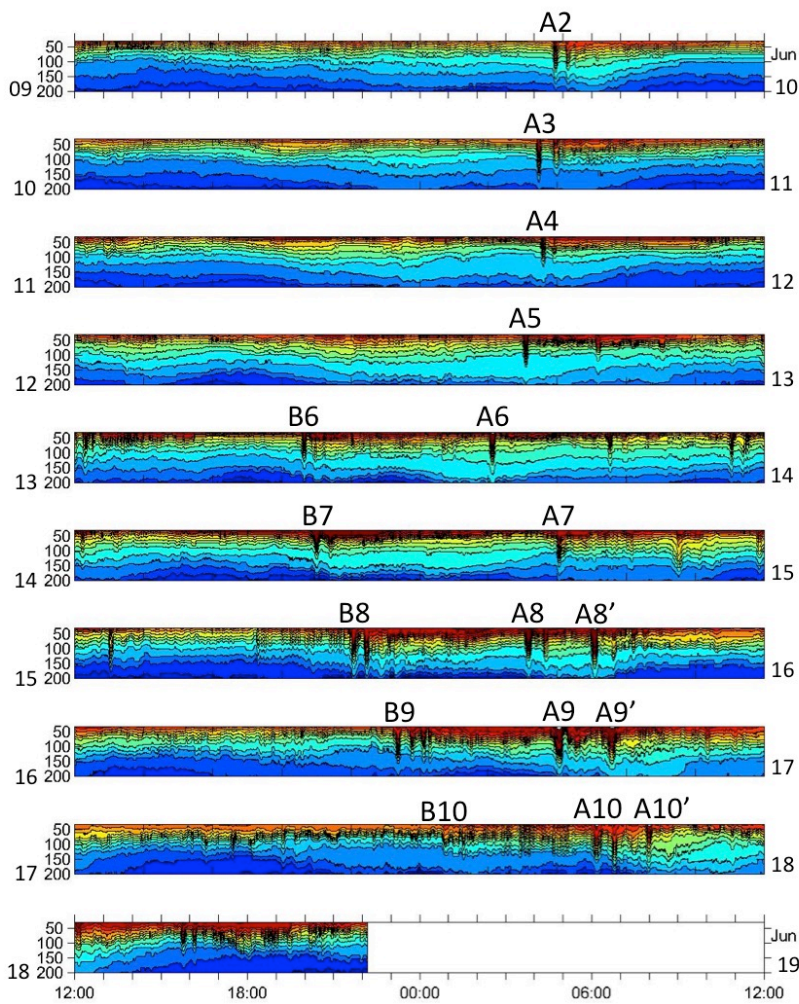
Moved up [4]: for the second cluster. Same-pair arrivals received the same number, i.e., B5 preceded A5 by about six hours, and so forth. Waves observed during the first

Moved (insertion) [5]

\$13 mooring RPO. This example thus demonstrates a local b-wave formation process
\$14 via steepening of the leading edge of the tidal front. We show subsequently that this
\$15 steepening temperature front was due to velocity convergence at the head of the
\$16 westward-propagating internal tide. The formation of a similar bore-like feature at
\$17 shallower depths (200 m – 120 m) was noted in the ASIAEX data [Duda et al., 2004]
\$18 but they did not make the connection to b-wave formation. Waves a1 and a2 lost
\$19 amplitude and formed packets as they shoaled between YPO2 and RPO. This
\$20 process will be compared with some recent theoretical ideas in the discussion
\$21 section. Wave a3 was small at YPO2 but gained amplitude as the tide progressed up
\$22 the slope. This is because the barotropic forcing in the Luzon Strait was weaker on
\$23 June 5 than on June 2-4 (ref. Figure 3). All the waves subsequently disappeared on
\$24 June 7-8 during neap tide in the Luzon Strait.

\$25
\$26 The second sequence during June 10-14 shows well developed A-wave packets
\$27 which originated from moderate but increasing remote forcing (Figure 6). Only A-
\$28 waves were observed until June 13 when the B-waves started to arrive. Wave B6
\$29 was weakly perceptible at YPO2 and increased in amplitude across the slope. The
\$30 temperature fluctuations induced by the A-waves increased across the slope and
\$31 reached a maximum of 7°C on June 11 at A3. The temperature gradients in the wave
\$32 fronts were again very steep, 1°C / min. The number of waves per packet increased
\$33 towards shallower water, most clearly in waves A2, A3, and A4. Two extraneous
\$34 solitary waves appeared trailing wave A5 on June 13 at CPO and RPO but were not
\$35 part of the A5 packet structure. Two similar waves appeared the next day trailing
\$36 wave A6 (Figure 7) and their origin is unclear.

\$37
\$38 The final sequence from June 14 to 18 was obtained during a period of maximal
\$39 forcing near spring tide at the source, and a very complicated field of NLIW emerged
\$40 (Figure 7). The B-waves were large and were evident at all the moorings. Wave B8
\$41 and B9 were solitary at YPO2 but had many waves per packet by the time they
\$42 reached RPO. The arrival timing was the same as the locally formed b-waves
\$43 (Figure 5) suggesting similar dynamics but faster/shorter development
\$44 time/distance when the forcing at the source was stronger. The A-waves continued
\$45 to grow at YPO2 during June 14-18. Interestingly, the temperature fluctuations due
\$46 to the largest waves did not increase monotonically as they traveled up the slope
\$47 from YPO2 to RPO. This is more clearly seen in a bar graph showing the maximum
\$48 amplitude of the isotherm of maximum displacement (Figure 8). Smaller waves
\$49 (June 9-12) gained amplitude as they shoaled. All waves larger than about 50 m
\$50



\$51
\$52
\$53
\$54
\$55
\$56
\$57
\$58
\$59
\$60

Figure 4. Temperature contour plots for mooring RPO from June 9 to 19, 2014. Each panel from top to bottom is one day centered on midnight, to capture both the A- and B-wave arrivals. The A-waves were prominent throughout this fortnightly cycle. The B-wave arrivals began on June 13, five days after the A-waves. The double A-waves (A8'-A10') arrived only during June 16-18. This and similar plots were used to label the waves in Figure 3.

Deleted: Figure 4a. Temperature contour plots for mooring RPO from May 31 to June 10, 2014. Each panel from top to bottom is one day centered on midnight, to capture both the a- and b-wave arrivals. The individual waves are labeled to match Figure 3. No waves arrived during June 7-8, corresponding to neap tide in the Luzon Straits. ¶ ... [2]

Deleted: b

Deleted: As in Figure 4a, only for the time period June 9 to June 19, 2014.

Deleted: (

Deleted:)

Deleted: (June 8)

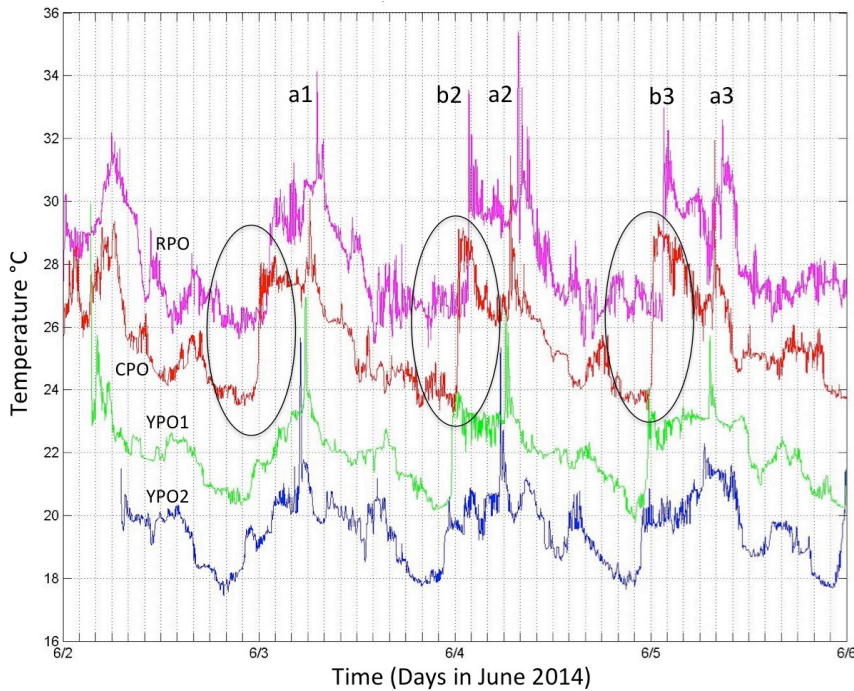
Deleted: Spring tide in the Luzon Straits was on June 14, thus the largest waves are expected two days later at the array.

Deleted: ¶ times between the B-waves and the A-waves was 6:30, 8:25, 6:15, and 5:50 on June 14-17 respectively. Had the June 15 A-wave fit the pattern and not arrived late, the time difference on that day likewise would have been. [3]

Moved up [5]: times between the B-waves and the A-8:25, 6:15, and 5:50 on June 14-17 respectively. Had the June 15 A-wave fit the pattern and not arrived late, the time difference on that day likewise would have been about 6 hours. They could possibly be produced by the

Deleted: 3.3 Wave Transformation Over the Slope ¶

¶ Many significant wave transformations were observed between the 386 m (YPO2) and the 266 m (RPO) isobaths over the upper continental slope. Three sections of the [4]

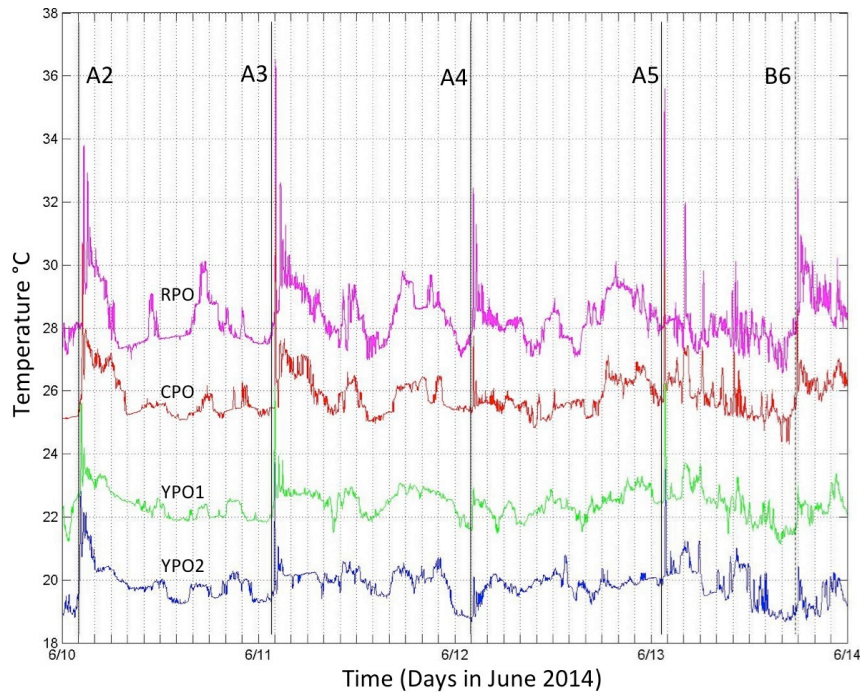


786
787
788
789
790
791
792
793
794
795
796
797
798
799
800
801
802
803
804
805
806
807

Figure 5. Temperature vs. time during June 2-6 at all four moorings across the continental slope. The observations are from 75m, 79m, 97m, and 99m from moorings RPO, CPO, YPO1, and YPO2 respectively. Each time series has been offset vertically by 2 °C for clarity. The black ellipses highlight the region of strong temperature fronts at CPO that subsequently broke and formed b-waves at RPO.

offshore (June 13-18) lost amplitude as they shoaled, most clearly between CPO and RPO, where the biggest change in bottom depth and slope occurred. This result is consistent with the numerical results of [Lamb and Warn-Varnas, 2015] who also found that smaller amplitude waves continued to gain amplitude into shallower water but the larger waves did not. This fundamental result, that NLIW first gain amplitude and then lose it as they shoal, is consistent with EKdV theory [Small, 2001; Vlasenko et al., 2005]. Note that all the wave amplitudes (Figure 8) were smaller than those observed previously over the continental slope 44, 87, and 145 km to the southwest [Ramp et al., 2004; Lien et al., 2014; Ramp et al., 2022]. This is because, as seen in hundreds of satellite images (typified by Figure 9), the NLIWs have maximum amplitude in the region just north of the Dongsha Plateau near 20°N decreasing both northward and southward from there. The Sand Dunes site is

- Deleted: a
- Deleted: much less
- Deleted: in the ASIAEX and WISE/VANS region located 43.7 km along the topography towards the southwest.
- Deleted: actually near the northeastern



813
814

815 *Figure 6. As in Figure 5, except during June 10-14, 2014. In this plot, the time series*
816 *have additionally been shifted relative to YPO2 by the propagation time between*
817 *moorings so that individual waves line up. The lag times used are 36.5 min for YPO1,*
818 *66.8 min for CPO, and 122.8 min for RPO.*

819

820 actually near the northeastern extremity of the wave crests as viewed in the
821 imagery: a bit farther to the northeast the waves vanished. A practical ramification
822 of this is that the undersea sand dunes were located in a region where the forcing
823 due to encroaching NLIWs was not maximal. Other factors such as the bottom slope
824 and sediment supply must also play an important role in determining the dune
825 formation location. ▾

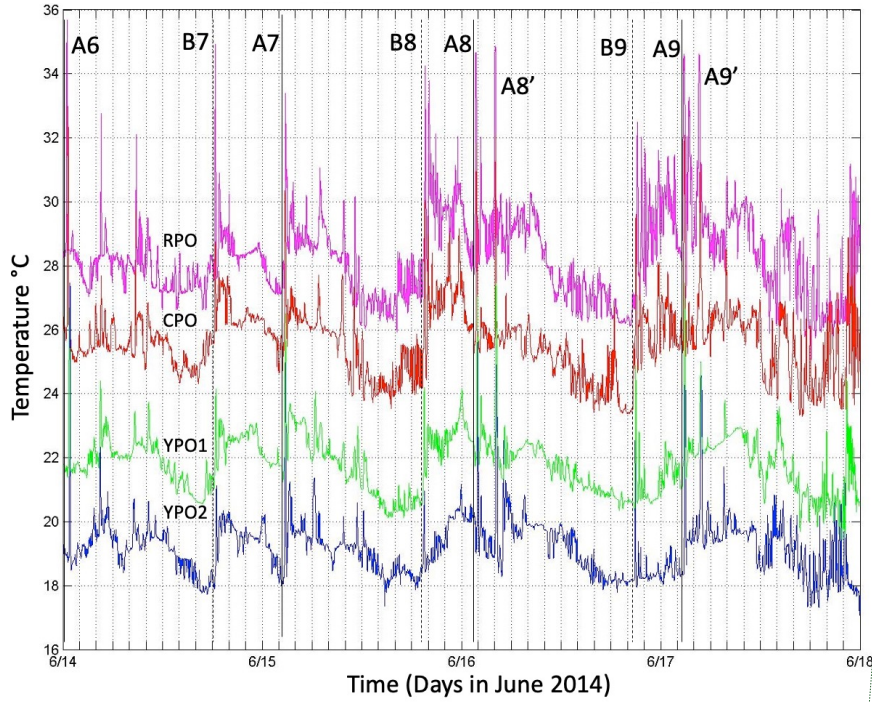
826

827 The double A-wave phenomenon mentioned earlier (Figure 4) was again evident in
828 Figure 7. These waves differed from the smaller waves trailing A5 and A6 in that
829 they were already well-developed by the time they arrived at YPO2. As in Figure 6,
830 many waves which were solitary at YPO2 formed packets as they crossed the array.
831 Waves B9, A9, and A9' can be clearly seen in the satellite ocean color imagery
832 (Figure 9). The timing of the imagery at 0310 is conveniently just as wave A9 was
833 impacting mooring YPO2. The B-wave packets and solitary nature of A9 and A9' are
834 easily seen in the image.

Deleted:

Deleted: b

837



838

839

840

841 *Figure 7. As in Figure 6 except for June 14-18.*

842

843 Two examples of velocity and temperature across the slope are shown to illustrate
 844 the difference between weakly and strongly forced waves. Mooring YPO1 is not
 845 shown since it was very similar to mooring YPO2 (Figure 10). The weaker case
 846 begins at YPO2 on June 3-4 (Figure 10, column 1) which shows a clear a-wave near
 847 0530 but no b-wave. Wave a2 was observed towards the rear of the
 848 northwestward-propagating internal tide (blue near the surface). The a-wave was
 849 traveling NW near the surface and in the opposite direction in the lower water
 850 column, with a nodal point near 100 m. While not obvious in temperature, the
 851 velocity plots show a weak second wave about 20 min behind the lead wave forming
 852 a 2-wave packet. By mooring CPO (column 2), located 7.3 km away, the leading edge
 853 of the internal tide had steepened to form a sharp front in both velocity and
 854 temperature near midnight on June 3. There was strong convergence in the upper

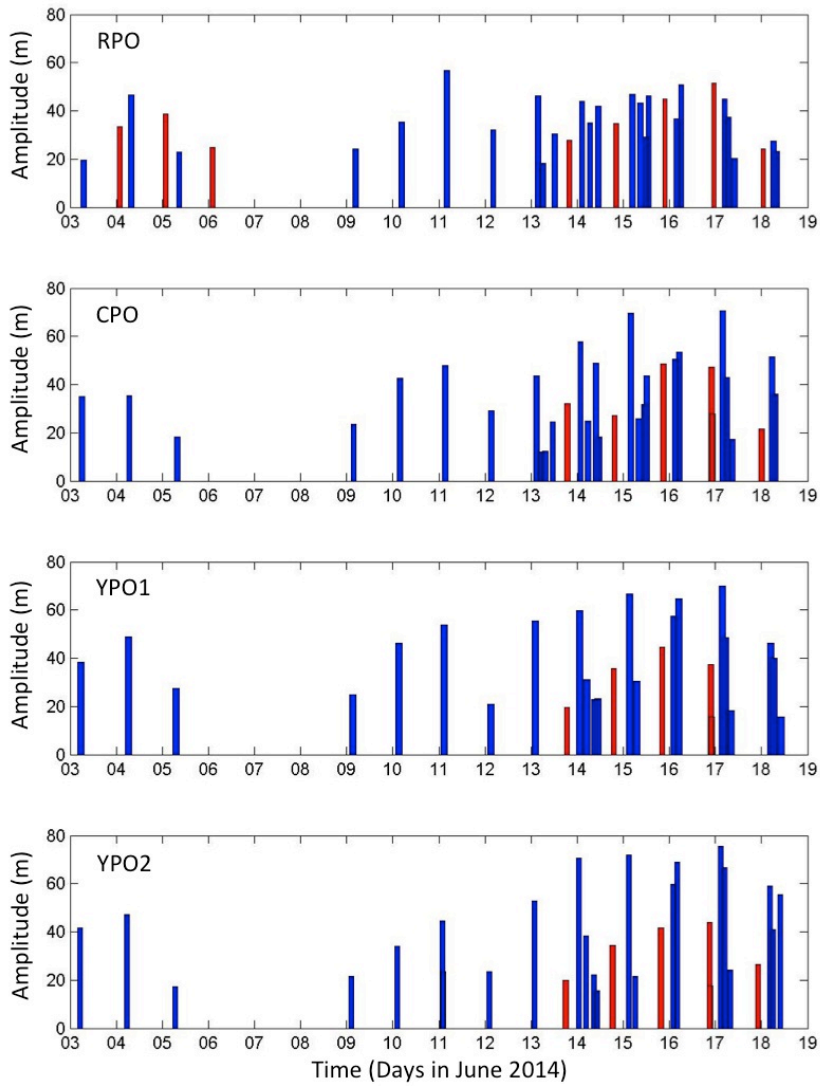
Moved down [6]: Two examples of velocity and temperature across the slope are shown to illustrate the difference between weakly and strongly forced waves. Mooring YPO1 is not shown since it was very similar to mooring YPO2. The weaker case begins at YPO2 ¶

Moved (insertion) [6]

Deleted: ¶

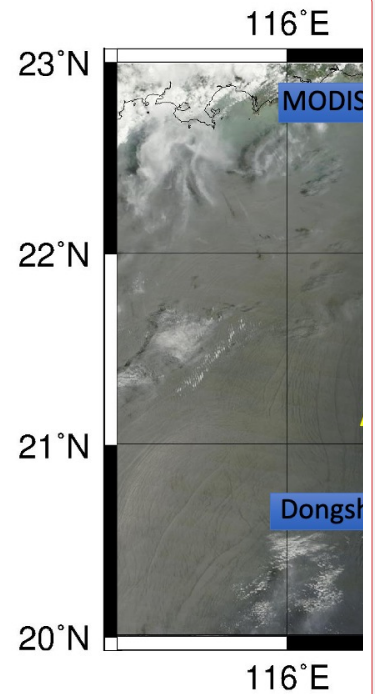
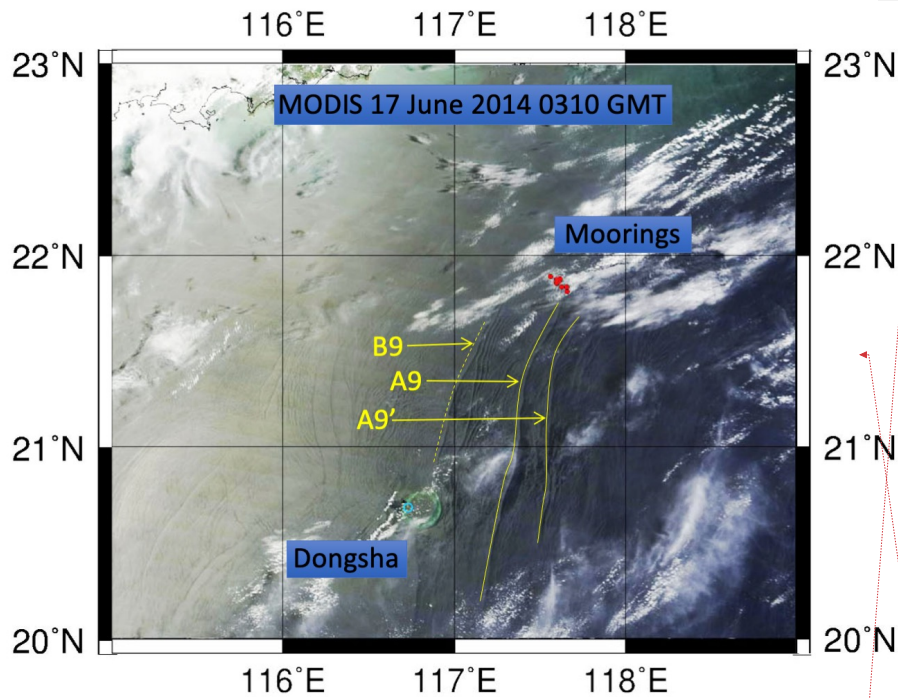
Deleted: 50 m with eastward flow (yellow) ahead of the front and westward flow (blue) behind it. A solitary b-wave appeared on this convergent front which was absent at YPO2. Wave a2 at CPO looked similar to YPO2, perhaps slightly stronger.

Moved down [7]: By mooring RPO, 5.7 km and 80 m farther up the slope (column 3), the b-wave increased in amplitude and formed a 2-wave packet, and the leading a-wave spawned a 4-wave packet. These waves were particularly clear in the v-component since the waves refracted towards the north as they propagated up the slope (Figure 1). The nodal point remained near 100 m for all the ¶



874
875
876
877
878
879
880

Figure 8. Bar graph of wave amplitudes across the slope. The amplitudes were calculated as deviations of the 20 °C isotherm from its mean position. The a-waves are indicated by blue bars and the b-waves by the red.



Deleted:
Formatted: Centered

Deleted:

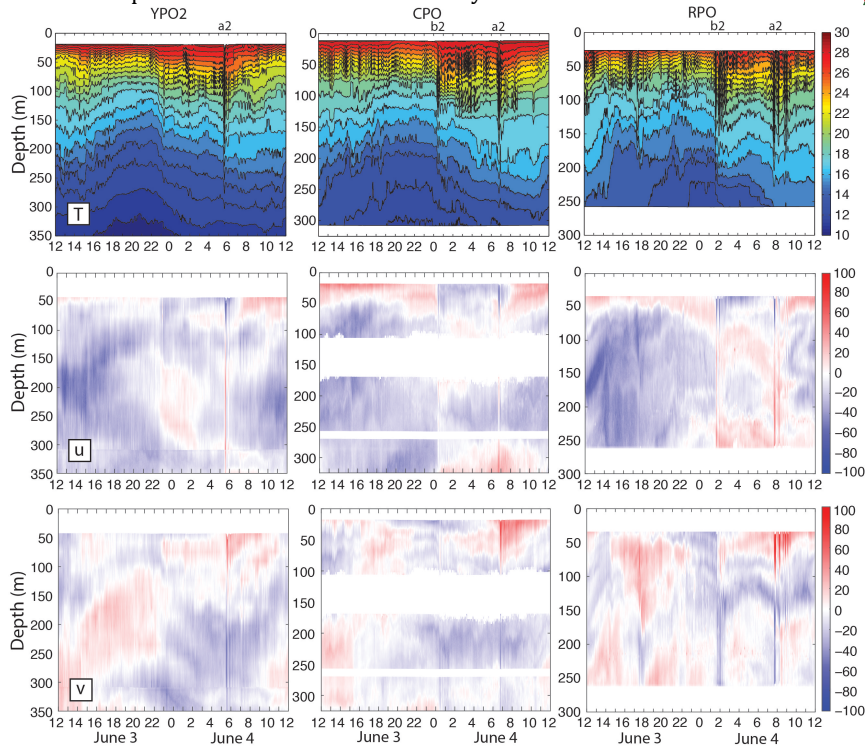
Moved (insertion) [7]

881
882
883
884
885
886
887
888
889
890
891
892
893
894
895
896
897
898
899
900
901

Figure 9. A sea surface ocean color image obtained at 0310 on June 17, 2014 from the Moderate Resolution Imaging Spectroradiometer (MODIS). The Sand Dunes moorings are indicated by the red dots. The site of the former ASIAEX and WISE/VANS mooring S7 is indicated by the yellow triangle. The surface signatures of NLIWs B9, A9, and A9' are indicated by the yellow arrows. Wave A9 was impinging upon mooring YPO2 at this moment, as seen in Figure 7.

50 m with eastward flow (red shades) ahead of the front and westward flow (blue shades) behind it. A solitary b-wave appeared on this convergent front which was absent at YPO2. Wave a2 at CPO looked similar to YPO2, perhaps slightly stronger. By mooring RPO, 5.7 km and 80 m farther up the slope (column 3), the b-wave increased in amplitude and formed a 2-wave packet, and the leading a-wave spawned a 4-wave packet. These waves were particularly clear in the v-component since the waves refracted towards the north as they propagated up the slope (Figure 1). The nodal point remained near 100 m for all the leading waves. Note that the background internal tide (most easily seen in the deep water) was diurnal at moorings YPO2 and CPO but became more semidiurnal at RPO. This indicates the presence of a locally generated tide at RPO where the bottom slope was steeper than at the other moorings farther offshore. In fact, the bottom slope at YPO2-CPO

904 (Figures 1, 2 right of the dotted white line) was critical to the diurnal tide while the
 905 slope at RPO (left of the dotted white line) was critical to the semidiurnal tide. The
 906 interaction of the tidal currents with the bottom is maximal where the slope of the
 907 tidal beams parallels the bottom and this likely contributes to the different nature of

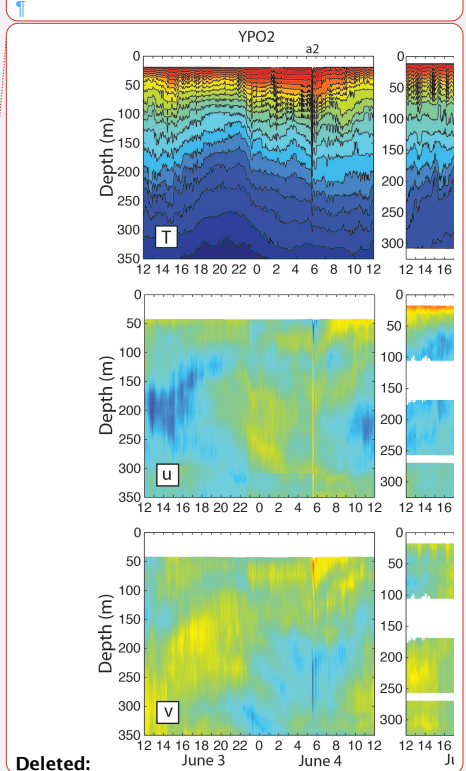


908
 909
 910 *Figure 10. Temperature (top), u-component of velocity (middle) and v-component of*
 911 *velocity (bottom) from 3-4 June 2014 from moorings YPO2 (left), CPO (center), and*
 912 *RPO (right). The wave propagation time between moorings was 67 min from YPO2 to*
 913 *CPO, and 56 min from CPO to RPO. Positive (u, v) represents (east, north) respectively.*
 914 *White space at mooring CPO indicates regions not sampled by the three ADCPs. These*
 915 *data were obtained during a period of moderate and declining tidal forcing, see*
 916 *Figures 3 and 5 for context.*

917
 918 the sand dunes offshore vs. onshore of the dotted white line (Figure 2). At all
 919 moorings, there was only one westward surface internal tide per day. The b-waves
 920 all emerged at the leading edge of this westward tide, while the a-waves emerged
 921 towards the rear, and this clear velocity signature represents another way to
 922 distinguish the two types of waves. The two wave arrivals were separated by 6:20

Moved down [8]: the sand dunes offshore vs. onshore of the dotted white line (Figure 2). This point is taken up further in a subsequent work.

Deleted: ¶



Deleted:

Moved (insertion) [8]

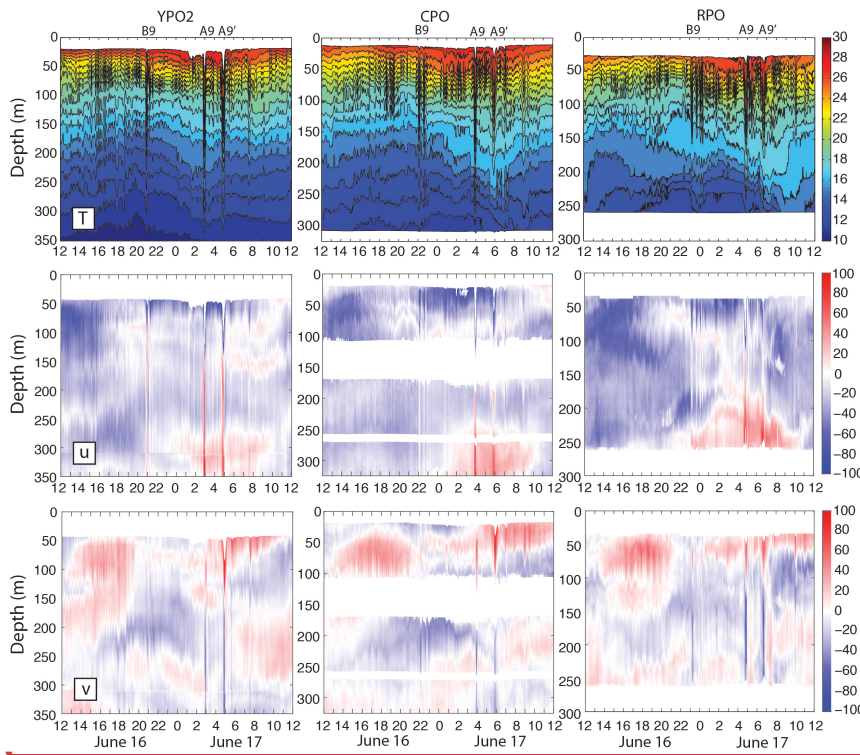
Deleted: This point is taken up further in a subsequent work.

931 on this day. The strongest bottom velocities were down-slope (southeast) and were
 932 greater in the NLIW than in the internal tide.
 933

934 The strong example (Figure 11) shows that unlike the previous example, both the B-
 935 wave packet and the A-wave packet had already formed by mooring YPO2 on June
 936 16-17. (Remember there is no dynamical significance to upper vs. lower case a, b:
 937 the lettering is chosen to remain consistent with the nomenclature established in
 938 the earlier figures and refers to the first and second cluster.) The waves were
 939 traveling in the same direction as the June 3-4 waves, but had a deeper nodal point
 940 located near 120-130 m. The A-wave in this case was a double A-wave mentioned
 941 earlier. These resembled individual waves rather than a packet in the usual sense.
 942 The two waves A9 and A9' were about the same amplitude: on this day the first
 943 wave (A9) was slightly larger but the opposite was true the day before (not shown).
 944 The A9' wave was slightly wider than the A9 wave. This may be due to constructive
 945

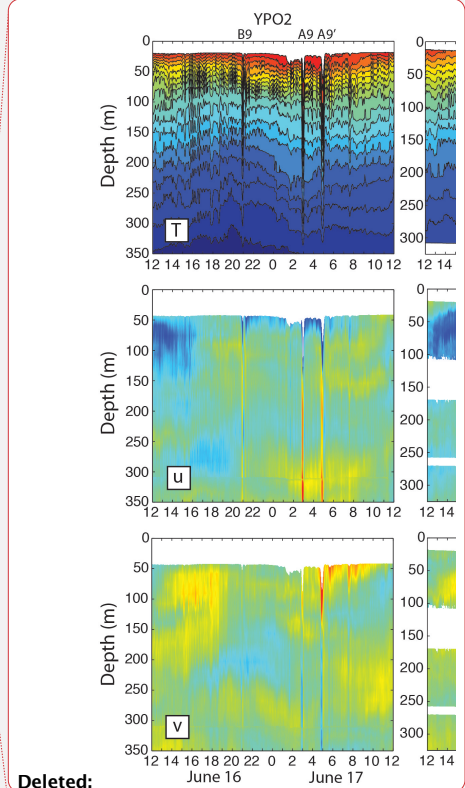
Moved (insertion) [9]

Deleted: interference with the tail of wave A9 which was just two hours ahead of it. Wave B9 formed a 2-wave packet at CPO (column 2) and a 3-wave packet at RPO (column 3). Wave A9 formed a 2-wave packet between moorings CPO and RPO. As before, the u-



946
 947
 948
 949

Figure 11. As in Figure 10, except for June 16-17, 2014. These data were obtained during a period of strong tidal forcing, see Figures 3 and 7 for context.



Deleted:
 Formatted: Centered
 Deleted: ¶

957
958 interference with the tail of wave A9 which was just two hours ahead of it. Wave B9
959 formed a 2-wave packet at CPO (column 2) and a 3-wave packet at RPO (column 3).
960 Wave A9 formed a 2-wave packet between moorings CPO and RPO. As before, the u-
961 component shows the B-wave was coming off the leading edge of the westward
962 surface tide (eastward bottom tide). The A9 wave grew out of the middle of the tide
963 and the A9' wave emerged from the trailing edge of the same westward internal
964 tide. The surface westward velocities exceeded 97 cm s⁻¹, 162 cm s⁻¹, and 153 cm s⁻¹
965 at YPO2, CPO, and RPO respectively. The eastward bottom velocities exceeded 20
966 cm s⁻¹, 85 cm s⁻¹, and 80 cm s⁻¹ respectively. The smaller lower layer velocities
967 below the nodal point were consistent with a thicker lower layer and with theory
968 [Lamb and Warn-Varnas, 2015]. The strongest bottom velocities outside the waves
969 were about half the wave velocities. Clearly the strongest bottom velocities
970 observed over the upper continental slope were generated by the passing NLIWs,
971 although these high velocities were very brief compared to the internal tide.
972 Referring once again to Figure 8, the B-wave (just before midnight on June 16)
973 started at YPO2 with just over 40 m amplitude and grew shoreward across the shelf.
974 In contrast, the much larger A-waves just after midnight on the 17th started out
975 with 70 – 75 m amplitude at YPO2 and lost amplitude across the shelf. This is
976 consistent with the earlier discussion surrounding Figure 10.

977
978 Many ordinary internal waves can be seen in Figure 11 in between the nonlinear
979 waves. These waves were likely generated by tropical cyclone Hagabus which
980 passed over the array on June 14-15 with winds exceeding 25 m s⁻¹.

981
982 On June 16 a packet of convex mode-2 waves appeared from 1500-2100 centered
983 near 60 m and extending from 50 to 100 m depth (Figure 11, bottom row). These
984 waves strengthened upslope from YPO2 to RPO and trailed the double-A waves
985 from the day before (not shown). There looked to be about 6 waves in the mode-2
986 packet at mooring RPO. All three of the double-A waves on 16, 17, and 18 June had
987 this feature associated with them. The observation is consistent with [Yang et al.,
988 2009, 2010] who observed mode-2 waves trailing mode-1 waves in the ASIAEX
989 region nearby and attributed this to the adjustment of shoaling mode-1 waves.
990 These observed wave transformations are now discussed further below in light of
991 the published theory for shoaling solitary waves.

992 4 Discussion

993 4.1 Theoretical Framework

994
995 In this section, the observed NLIW characteristics are compared with laboratory and
996 numerical studies to determine what kind of changes might be expected as the waves
997 shoal over the sand dunes region. The possibilities include adiabatic shoaling, dispersion,
998 breaking, and conversion to waves of elevation. The latter may be easily ruled out for
999 this study since this only happens when the nonlinear coefficient α from the KdV
1000 equation changes sign, which typically takes place between 100 – 120 m depth over the
1001

Moved up [9]: the lettering is chosen to remain consistent with the nomenclature established in the earlier figures and refers to the first and second cluster.) The waves were traveling in the same direction as the June 3-4 waves, but had a deeper nodal point located near 120-130 m. The A-wave in this case was a double A-wave mentioned earlier. These resembled individual waves rather than a packet in the usual sense. The two waves A9 and A9' were about the same amplitude: on this day the first wave (A9) was slightly larger but the opposite was true the day before (not shown). The A9' wave was slightly wider than the A9 wave. This may be due to constructive interference with the tail of wave A9 which was just two hours ahead of it. Wave B9 formed a 2-wave packet at CPO (column 2) and a 3-wave packet at RPO (column 3). Wave A9 formed a 2-wave packet between moorings CPO and RPO. As before, the u-

Deleted: *The physics of shoaling waves*

Deleted: ¶

The response of shoaling NLIWs over a sloping bottom depends critically on three factors: the bottom slope, wave amplitude, and thermocline depth [Small, 2001; Vlasenko and Hutter, 2002; Lamb, 2002; Vlasenko and Stashchuk, 2007; Grimshaw et al., 2014; Lamb and Warn-Varnas, 2015]. Over very slight slopes, waves shoal adiabatically with little change in form. The wave amplitudes first increase gradually and then rapidly decrease, with the depth of maximum amplitude depending on the details of the wave's initial amplitude, stratification, and bottom slope [Lamb and Warn-Varnas, 2015]. For the ASIAEX region nearby, they found the depth of maximum amplitude to be between 400-300 m. The width of the wave is inversely proportional to the amplitude, so the waves become wider once the amplitude starts to decrease. ¶

¶ As the bottom steepens, or alternatively the wave amplitude increases, a shoaling solitary wave tends to form packets via the formation of a trailing dispersive tail. When the bottom is steeper still, the combination of bottom slope, wave amplitude, and fractional upper layer thickness (set by the bottom depth and undisturbed thermocline depth) determine the onset of wave breaking and/or reflection. These concepts can be quantified: using a fully nonlinear two-dimensional model with continuous stratification, Vlasenko and Hutter [2002] studied shoaling solitary waves using bottom topography and stratification appropriate for the Andaman and Sulu Seas. As the wave shoals, the trough slows down relative to the surface, which causes the leading edge of the wave to flatten out and the back of the wave to steepen. The wave effectively breaks (from the back) when the orbital velocity (u) exceeds the propagation speed (C_p). This concept has also been observed in the field [Lien et al., 2012; 2014]. By means of multiple model runs varying the bottom slope and non-dimensional wave amplitude, [Vlasenko and Hutter, 2002] established a generalized criteria to determine the wave parameter space for which breaking or dispersion will occur (their Figure 8). The criteria is that: ¶ ... [5]

1191 layer. Such bottom velocities were commonly observed and are easily enough to
1192 produce both bedload and suspended sediment transport among the dunes [Reeder
1193 et al., 2011]. The w-profile was nearly symmetric at $\pm 0.25 \text{ m s}^{-1}$, downward ahead of
1194 the wave and upward behind it, with the maxima located near mid-depth. One or
1195 possibly two trailing waves were observed: the first was centered near 4:48 and had
1196 vertical velocities of $\pm 0.8 \text{ m s}^{-1}$ while the second was near 5:00 with vertical
1197 velocities of just a few cm s^{-1} . A fourth wave-like feature was observed in the
1198 temperature plot near 5:20 but it cannot be discerned in the velocity structure. To
1199 summarize, wave A3 consisted of a primary wave and 2-3 trailing waves about 30
1200 min behind. The wave was symmetric in velocity and temperature with no sign of
1201 breaking or trapped core formation.

Deleted: c

Deleted: c

Deleted: The velocity structure had open contours all the way up the minimum depth of the observations, with a maximum of 104 cm s^{-1} which is \ll the local propagation speed of 1.69 cm s^{-1} .

Deleted: a

1203 The largest wave observed was wave A9 on June 17. This wave showed several
1204 characteristics of breaking or near-breaking waves (Figure 13). The back side of the
1205 wave was steeper than the leading side, and the jagged temperature contours in the
1206 wave core were indicative of breaking and/or mixing. A “pedestal” was starting to
1207 form behind the wave as described by [Lamb and Warn-Varnas, 2015]. Several
1208 more smaller depression waves were emerging from the “pedestal.” The velocity
1209 contours were likewise asymmetric and showed a subsurface maximum near 60-70
1210 m which was about 0.20 m s^{-1} greater than the surface. This is typical of waves with
1211 trapped cores [Lien et al, 2012, 2014; Lamb and Warn-Varnas, 2015]. The
1212 maximum near-surface velocity was 1.55 m s^{-1} , which was close to the local phase
1213 speed (1.60 m s^{-1}). It is possible that the surface velocities above 20 m depth were
1214 slightly larger but were not observed. At site CPO, this same wave had a maximum
1215 velocity of 1.80 m s^{-1} , also very close to the local phase speed. The vertical velocities
1216 were actually smaller than wave A3, at -12 and $+20 \text{ cm s}^{-1}$ with at least two and
1217 possibly more of the trailing depression waves visible as down/up pairs. To
1218 summarize, this wave appears to be about to break or just starting to break,
1219 however, this wave was the exception rather than the rule: only one such wave was
1220 observed. It is possible that the trailing double-A waves A8' and A9' might also meet
1221 these criteria, however their form was distorted by interference from the trailing
1222 packet of the leading A8 and A9 waves two hours earlier, making their
1223 characteristics difficult to discern.

Deleted: c

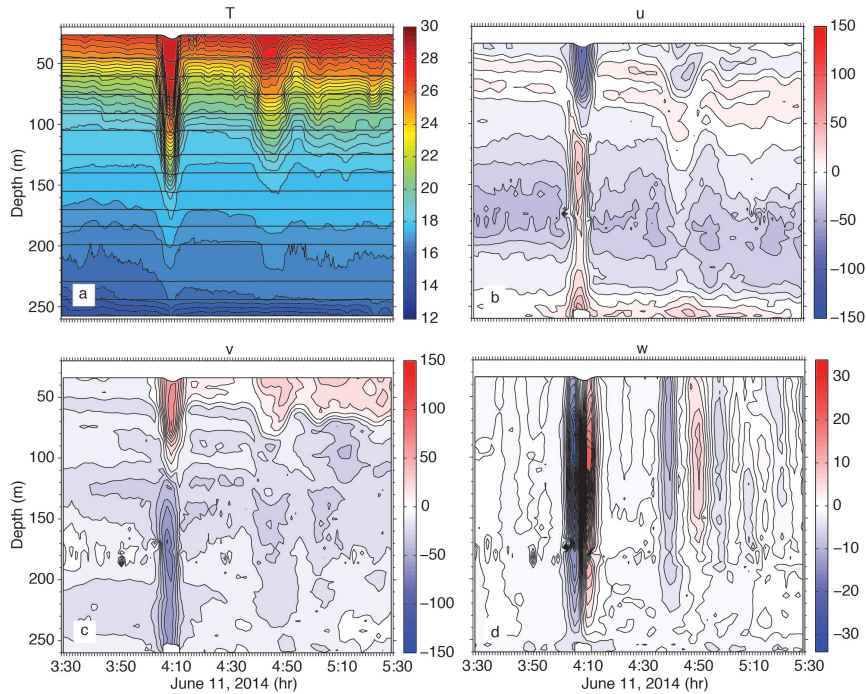
Deleted: c

Deleted: c

Moved (insertion) [10]

1224
1225 It is worth noting that subsurface velocity maximum in the wave may be caused by
1226 phenomena other than wave breaking. Tropical cyclone Hagabus passed over the
1227 array on June 14-15 and forced strong near-surface currents which opposed the
1228 wave velocities. This was especially obvious on June 15 (not shown) when
1229 westward currents at 80 m depth in wave A7 exceeded the surface currents by over
1230 0.80 m s^{-1} at RPO and by over 1.00 m s^{-1} at CPO. This likely explains why wave A7
1231 arrived 2 hours late with respect to waves A6 and A8 (Figure 4). The storm also left
1232 behind a surface mixed layer 40 m deep which lingered to the end of the record.
1233 This means all the largest waves forced near spring tide propagated into a region
1234 with an unusually deep surface mixed layer. The effect of this is to severely limit
1235 wave breaking [Lamb, 2002]. In fact, the scenario described above in the results
1236 section rather closely resembles the model results of [Lamb, 2002] when a surface

1247



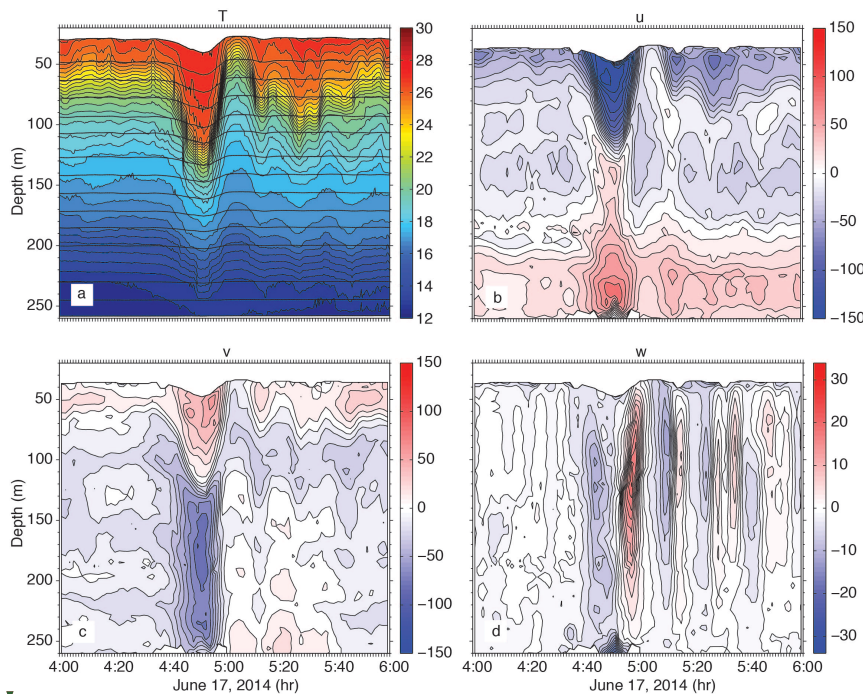
1248
1249
1250
1251
1252
1253
1254
1255
1256
1257
1258
1259
1260
1261
1262
1263
1264
1265
1266
1267
1268

Figure 12. a) temperature, b) u-component of velocity (positive east), c) v-component of velocity (positive north), and vertical velocity (positive up) for wave A3 on June 11, 2014. This rank-ordered packet with a symmetrical leading wave typifies most of the type-a waves observed during the experiment.

mixed layer was added (their Figure 10). The shoaling solitary wave in the model produced a second trailing solitary wave, followed by the dispersive tail of mode-1 depression waves, followed by a packet of mode-2 waves. The observations reported here closely resembled this pattern not only on June 16-18, but also on June 3-5 trailing waves a1 and a2.

We conclude that most of the packets that formed as the waves traveled up the slope from YPO2 to RPO were formed by dispersion rather than wave breaking. Rotational effects seem locally unimportant, given that the packets formed in just two hours while the local inertial period was 32 hours. Rotation may have played a role farther offshore, establishing the initial perturbations (inertial gravity waves) that then grow and become a trailing packet as the waves shoal [Grimshaw et al.,

Moved up [10]: wave appears to be about to break or just starting to break, however, this wave was the exception rather than the rule: only one such wave was observed. It is possible that the trailing double-A waves A8' and A9' might also meet these criteria, however their form was distorted by interference from the trailing packet of the leading A8 and A9 waves two hours earlier, making their characteristics difficult to discern. ↑



Deleted: It is worth noting that subsurface maxima in the wave may be caused by phenomena other than wave breaking. Tropical cyclone Hagabus passed over the array on June 14-15 and forced strong near-surface currents which opposed the wave velocities. This was especially obvious on June 15 (not shown) when westward currents at 80 m depth in wave A7 exceeded the surface currents by over 80 cm s^{-1} at RPO and by over 100 cm s^{-1} at CPO. This likely explains why wave A7 arrived 2 hours late with respect to waves A6 and A8 (Figure 4b). The storm also left behind a surface mixed layer 40 m deep which lingered to the end of the record. This means all the largest waves forced near spring tide propagated into a region with an unusually deep surface mixed layer. The effect of this is to severely limit wave breaking [Lamb, 2002]. In fact, the scenario described above in the results section rather closely resembles the model results of [Lamb, 2002] when a surface mixed layer was added.

Moved (insertion) [11]

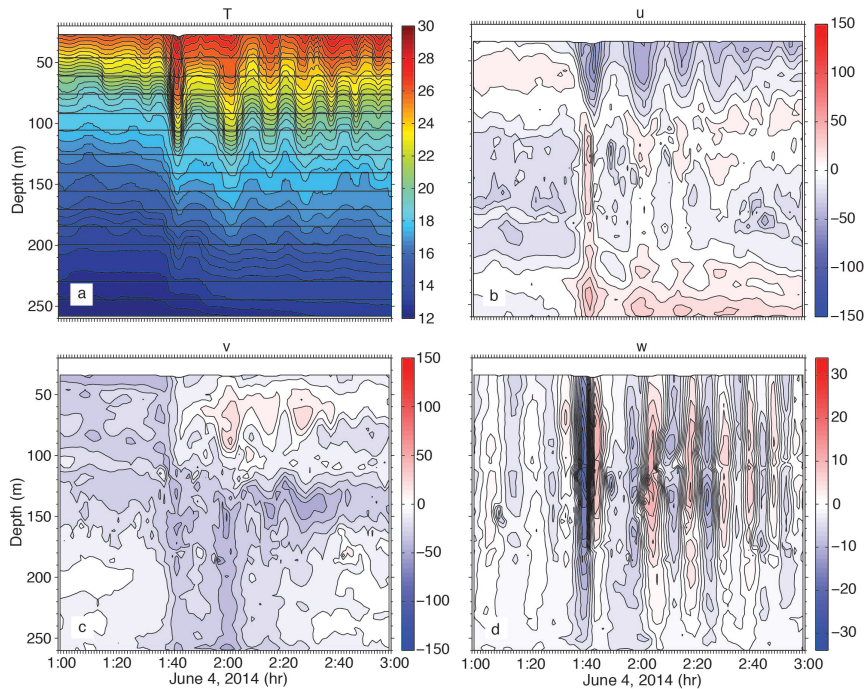
Moved (insertion) [12]

1277
1278
1279
1280
1281
1282
1283
1284
1285
1286
1287
1288
1289
1290
1291
1292
1293
1294
1295
1296
1297
1298

Figure 13. As in Figure 12, but for wave A9 on June 17, 2014. The steepening back side and subsurface velocity maximum suggest breaking or imminent breaking.

2014]. We are not able to investigate this effect without observations in deep water. Trailing undular bores of the sort modeled by [Grimshaw et al., 2014] by including rotation were not observed, but are likely not observable since in the real ocean, the waves arrive periodically and the trailing undular bores would be destroyed by each subsequent arriving NLIW before they have a chance to develop. It is most likely then an imbalance between nonlinearity and dispersion that causes the new trailing waves to form [Vlasenko and Hutter, 2002; Lamb and Warn-Varnas, 2015]. The large lead ISW in the Sand Dunes array never split in two, but rather slowly decreased in amplitude as energy was transferred to the dispersive tail. Phenomena such as wave splitting and breaking likely took place inshore of the sand dunes array in the vicinity of the 150 m isobath, as was observed previously at the ASIAEX site nearby.

The situation for the locally formed b-waves (b2-b4) was completely different. These waves were non-existent at YPO2 but formed well-defined, evenly spaced packets by the time they reached RPO (Figure 14). For wave b2 on June 4, six waves



Moved up [11]: waves forced near spring tide propagated into a region with an unusually deep surface mixed layer. The effect of this is to severely limit wave breaking [Lamb, 2002]. In fact, the scenario described above in the results section rather closely resembles the model results of [Lamb, 2002] when a surface mixed layer was added (their Figure 10). The shoaling solitary wave in the model produced a second trailing solitary wave, followed by the dispersive tail of mode-1 depression waves, followed by a packet of mode-2 waves. The observations reported here closely resembled this pattern not only on June 16-18, but also on June 3-5 trailing waves a1 and a2. ¶

¶ We conclude that most of the packets that formed as the waves traveled up the slope from YPO2 to RPO were formed by dispersion rather than wave breaking. Rotational effects seem locally unimportant, given that the packets formed in just two hours while the local inertial period was 32 hours. Rotation may have played a role farther offshore, establishing the initial perturbations (inertial gravity waves) that then grow and

Deleted: waves forced near spring tide propagated into a region with an unusually deep surface mixed layer. The effect of this is to severely limit wave breaking [Lamb, 2002]. In fact, the scenario described above in the results section rather closely resembles the model results of [Lamb, 2002] when a surface mixed layer was added (their Figure 10). The shoaling solitary wave in the model produced a second trailing solitary wave, followed by the dispersive tail of mode-1 depression waves, followed by a packet of mode-2 waves. The observations reported here closely resembled this pattern not only on June 16-18, but also on June 3-5 trailing waves a1 and a2. ¶

¶ We conclude that most of the packets that formed as the waves traveled up the slope from YPO2 to RPO were formed by dispersion rather than wave breaking. Rotational effects seem locally unimportant, given that the packets formed in just two hours while the local... [6]

Moved up [12]: 2014). We are not able to investigate this effect without observations in deep water. Trailing undular bores of the sort modeled by [Grimshaw et al., 2014] by including rotation were not observed, but are likely not observable since in the real ocean, the waves arrive periodically and the trailing undular bores would be destroyed by each subsequent arriving NLIW before they have a chance to develop. It is most likely then an imbalance between nonlinearity and dispersion that causes the new trailing waves to form [Vlasenko and Hutter, 2002; Lamb and Warn-Varnas, 2015]. The large lead ISW in the Sand Dunes array never split in two, but rather slowly decreased in amplitude as energy was transferred to the dispersive tail. Phenomena such as wave splitting and breaking likely took place inshore of the sand dunes array in the vicinity of the 150 m isobath, as was observed previously at the ASIAEX site nearby. ¶

1318
1319 **Figure 14.** As in Figure 12, except for wave b2 on June 4, 2014. This example typifies
1320 waves formed locally by breaking of the tidal front between moorings YPO and RPO.
1321

1322 can be clearly seen in T and w, with most all the horizontal velocity in u, that is these
1323 waves were traveling westward. The amplitude of the lead wave was about 40 m,
1324 the near surface velocity 60 cm s^{-1} westward, and near-bottom velocity 40 cm s^{-1}
1325 eastward. The waves were formed all at once by the collision and breaking of the
1326 westward internal tide with the off-slope propagating eastward tide. This is a
1327 different mechanism than that described for shoaling ISWs in the literature.

1328
1329 **4.2 Energy and energy flux**
1330

1331 The data set provides an opportunity to observe how the horizontal kinetic (HKE)
1332 and available potential (APE) energy in the high-frequency nonlinear internal waves
1333 changes as the waves propagate up a gentle slope. In turn, the energy pathways
1334 provide some insight to the dynamics underlying the wave transformation process.
1335 The theoretical expectation for linear and small-amplitude nonlinear internal waves
1336 is that the energy will be equipartitioned for freely propagating long waves away
1337 from boundaries. This is not the case however for finite amplitude nonlinear,

1468 nonhydrostatic internal solitary waves whose KE typically exceeds the PE by a factor
1469 of 1.3. This result was found theoretically via exact solutions to the fully nonlinear
1470 equations of motion [Turkington et al., 1991] and has also been noted
1471 observationally [Klymak et al., 2006; Moum et al., 2007]. Thus, the KE is expected to
1472 slightly exceed the PE for the waves arriving at mooring YPO2. For shoaling NLIW
1473 however, the flux of PE greatly exceeds the flux of KE which causes the PE to exceed
1474 the KE in shallower water [Lamb, 2002; Lamb and Nguyen, 2009]. This is because
1475 the flux of PE remains nearly constant while the KE flux decreases as the upper and
1476 lower layer thicknesses become more equal. Shoaling waves observed in the
1477 Massachusetts Bay displayed this property [Scotti et al., 2006]. Thus, a shift from
1478 greater KE to greater PE might be expected as the waves shoal from YPO2 to RPO,
1479 although it depends on the details of the wave amplitude, stratification, bottom
1480 slope, etc.

1481
1482 To compute the energies and energy fluxes from moorings, time series of density
1483 and velocity which are uniform in space and time are required. Moorings RPO and
1484 CPO had good coverage of temperature and salinity in the vertical ([Appendix A,](#)
1485 Table 1) however moorings YPO1 and YPO2 sampled temperature only. Two
1486 methods to compute the density at YPO1 and YPO2 were explored. The first used a
1487 constant salinity (34.42, the vertical average from a nearby CTD cast) paired with
1488 the observed temperature at each sensor to compute density. This method assumes
1489 that most of the density variability comes from the temperature fluctuations rather
1490 than salinity. The second method used the salinity profiles from all the CTD casts
1491 taken during the cruise to compute a mean T/S curve, which was then used as a
1492 look-up table to determine the salinity to use with each observed temperature. The
1493 CTD casts were all within 12 km of each other and were thus treated as a time
1494 series. The profiles fell into two groups, namely before tropical storm Hagabus
1495 passed by on June 14, with little-to-no surface mixed layer, and after the storm when
1496 the mixed layer was about 40-50 m deep. Thus, two mean T/S curves were actually
1497 used, one from before the storm and one after. The benchmark for these methods
1498 was to compare the density calculated using the T/S curves with the actual density
1499 calculated using the observed salinity on moorings RPO and CPO. The APE
1500 computed using the mean T/S curve was found to agree much better with the
1501 observations than the APE computed using a constant value for the salinity. Both
1502 techniques were slight underestimates of the true APE, but the T/S method much
1503 less so than the constant method. For this reason, the mean T/S curves were used
1504 to compute the density time series, and thus APE for moorings YPO1 and YPO2.

1505
1506 The observed time series also had velocity gaps of varying severity in the water
1507 column due to the range limitations of the ADCPs. Mooring CPO had a mid-depth
1508 gap spanning roughly 110-170m and a second smaller gap from 255-265m (see
1509 Figures 10 and 11). These gaps were filled using the least squares fit normal mode
1510 techniques described in [Nash et al., 2005]. Theoretically as many as seven modes
1511 (number of instruments in the vertical - 1) were possible, but the most stable
1512 results were achieved with just three modes. No attempt was made to fill in the

1513 upper 20 m of the water column where both velocity and temperature were
 1514 unsampled by the moorings.

1515

1516 Once clean time series were available to operate on, the energies and energy fluxes
 1517 were computed from the data via established techniques [Nash *et al.*, 2005, 2006;
 1518 Lee *et al.*, 2006]. The baroclinic velocity and pressure fluctuations induced by the
 1519 waves were first computed as

1520

$$1521 \quad \bar{u}'(z,t) = \bar{u}(z,t) - \bar{u}(z) - \frac{1}{H} \int_{-H}^0 [\bar{u}(z,t) - \bar{u}(z)] dz \quad (1)$$

1522

1523 and

1524

$$1525 \quad p'(z,t) = g \int_z^0 \rho'(\zeta,t) d\zeta - \frac{g}{H} \int_{-H}^0 \int_z^0 \rho'(\zeta,t) d\zeta dz \quad (2)$$

1526

1527 where

1528

$$1529 \quad \rho'(z,t) = \rho(z,t) - \bar{\rho}(z) \quad (3)$$

1530

1531 is the density anomaly with respect to the time-mean density profile. In equations
 1532 (1) and (2), the last term satisfies the baroclinicity requirement that the primed
 1533 quantities integrate to zero over the entire water column [Kunze, *et al.*, 2002]. Over
 1534 bars indicate temporal means. The HKE and APE can then be computed as

1535

$$1536 \quad HKE = \rho_0 (u'^2 + v'^2) / 2 \quad (4)$$

1537

$$1538 \quad APE = \frac{1}{2} \frac{g^2 \rho'^2}{\rho_0 N^2} \quad (5)$$

1539

1540 where ρ_0 is the mean density, g is the acceleration of gravity and N^2 is the buoyancy
 1541 frequency.

1542

1543 The energy flux due to highly nonlinear internal waves is given by

1544

$$1545 \quad \bar{F}_E = \bar{u}'(p' + HKE + APE) \quad (6)$$

1546

1547 where the first term on the right is the pressure work and the second and third
 1548 terms represent the advection of horizontal kinetic and available potential energy
 1549 density [Nash *et al.*, 2012]. For the small amplitude, linear, hydrostatic case the flux
 1550 equation is often approximated as the first term only

1551

$$1552 \quad \bar{F}_E = \bar{u}'p' \quad (7)$$

1552
1553 but since it is not obvious that this approximation is valid for the strongly nonlinear
1554 shoaling waves observed in the sand dunes region, all three terms of the flux
1555 equation were computed.
1556

1557 The resulting changes in the wave energy distribution across the slope depended on
1558 the wave amplitude (Figure 15). For waves up to and including A3 on June 11, the
1559 APE exceeded HKE offshore and continued to increase up the slope. This is
1560 interpreted to mean the waves were still growing and had not yet reached
1561 maximum amplitude. Smaller waves can penetrate farther upslope adiabatically
1562 than larger waves. Wave A4 was anomalously small for which no obvious
1563 explanation has been found. Perhaps the wave was obliterated by the leading edge
1564 of tropical storm Hagabus. Starting with wave A5 on June 13, as the remote
1565 barotropic tidal forcing continued to increase, the HKE exceeded APE at YPO2 by a
1566 factor averaging 1.7 and increased to its maximum value at mooring YPO1. This
1567 ratio is even larger than the theoretical expectation of 1.3 [Turkington 1991; Lamb
1568 and Nguyen, 2009] and indicates highly nonlinear waves with large amplitudes.
1569 Between CPO and RPO, there was a dramatic change when the APE increased and
1570 the HKE sharply decreased, resulting in greater APE than HKE at mooring RPO
1571 (Figure 15a). The energy ratio at RPO (Figure 15f) was commonly three to four but
1572 suddenly decreased sharply with the arrival of wave A6 on June 14 and remained
1573 near one for the remainder of the time series. This is attributed to the increased
1574 surface mixed layer depth as the tropical storm went by which wiped out the upper
1575 ocean stratification and reduced the APE. The total energies (Figure 15e) integrated
1576 both vertically and over a wavelength, followed an envelope consistent with the
1577 remote tidal forcing and maxed out at around 250 MJ m⁻¹. This was less than half
1578 the energy (550 MJ m⁻¹) previously reported over the Dongsha Plateau [Lien et al.,
1579 2014] where the maximum observed wave amplitudes exceeded 150 m vs. 80 m
1580 here. The total energy appears approximately conserved across the slope for many
1581 of the waves as indicated by color bars of approximately equal length (Figure 15e).
1582 The losses in HKE were compensated for by the increases in APE, in reasonable
1583 agreement with theory and numerical simulations [Lamb and Nguyen, 2009; Lamb
1584 and Warn-Varnas, 2015]. For the larger waves however, such as a1, A6, A8', A9, and
1585 A9' the total energy decreased upslope (Figure 15e). The HKE was lost much faster
1586 than the APE was gained. This is attributed to strong dissipation over the rough
1587 bottom in the dune field [Helfrich et al., 2022].

1588
1589 In the simplest sense the energy flux is just the energy times the group velocity (or
1590 phase velocity for non-dispersive waves). Since the phase velocity varied from 1.87
1591 m s⁻¹ between YPO2 and YPO1 to 1.69 m s⁻¹ from CPO to RPO, the flux/energy ratio
1592 is expected to vary little across the slope and the flux patterns should resemble that
1593 of the total energies. This is indeed the case as seen by comparing the envelope of
1594 the curves for the total flux (Figure 16b) and the total energy (Figure 15e). The
1595 vertically integrated flux tends to decrease upslope primarily due to the decreasing
1596 water depth. Of greater interest is the change in the various terms of equation (6).

Deleted: c

Deleted: f

Deleted: 0

Deleted: exceptions however: wave a1 on June 3 and A7 on June 15 had much less energy arriving at RPO than was present at CPO. This may have been due to tropical storm Hagabus for the June 15 wave, but the reason is not obvious for the June 3 wave. Altogether the results are consistent with the idea of greater HKE in the larger incident waves with energy transferring from HKE to APE as the waves shoaled. The results are

Deleted: .

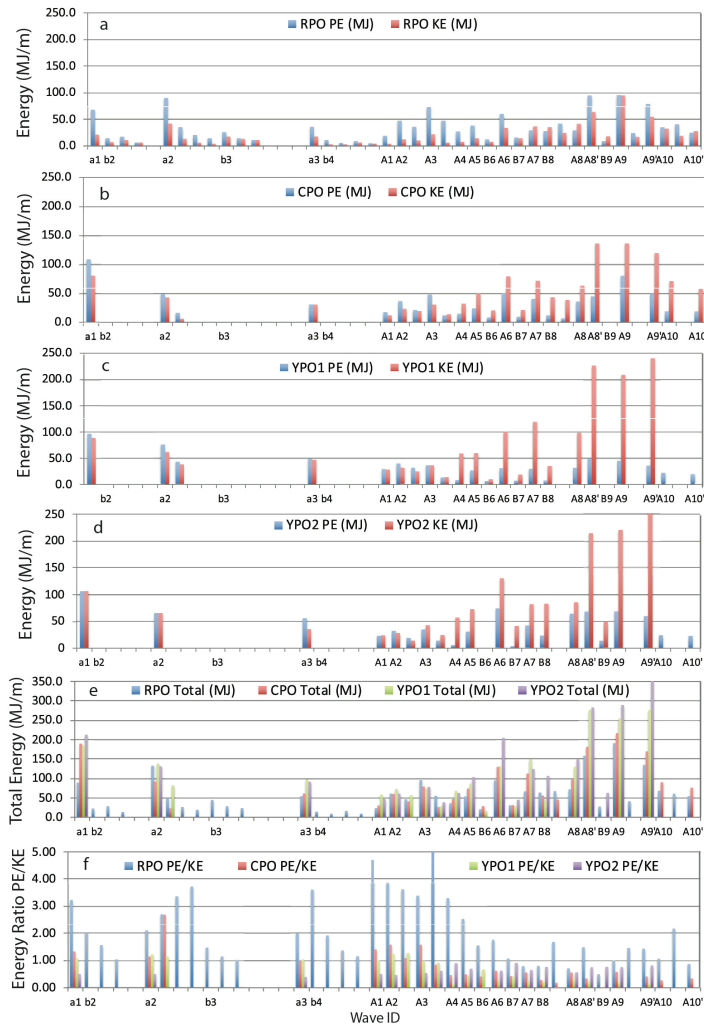
Moved (insertion) [14]

Deleted: a

Deleted: f

Deleted: The pressure work is indeed the largest term but not by much: The PW comprised 57%, 56%, 43%, and 52% of the total flux at YPO2, YPO1, CPO, and RPO. There were exceptions however: wave a1 on June 3 and A7 on June 15 had much less energy arriving at RPO than was present at CPO. This may have been due to tropical storm Hagabus for the June 15 wave, but the reason is not obvious for the June 3 wave. Altogether the results are consistent with the idea of greater HKE in the larger incident waves with energy transferring from HKE to APE as the waves shoaled. The results are in reasonable agreement with theory and numerical simulations [Lamb and Nguyen, 2009; Lamb and Warn-Varnas, 2015]. ¶

Moved (insertion) [13]



1624
1625

1626 *Figure 15. Energy transformations across the slope. The total HKE and APE,*
1627 *computed by integrating the wave energy both vertically and horizontally at moorings*
1628 *RPO, CPO, YPO1, and YPO2 are shown in panels a-d respectively. The total pseudo-*
1629 *energy (HKE + APE) at all four moorings is shown for each wave in panel e, and the*
1630 *APE/HKE ratio in panel f.*

1631
1632
1633
1634
1635
1636
1637
1638
1639
1640
1641
1642
1643
1644
1645
1646
1647
1648
1649
1650
1651
1652
1653
1654
1655
1656
1657
1658
1659
1660
1661
1662
1663
1664
1665
1666
1667
1668
1669
1670
1671
1672
1673
1674
1675
1676

The pressure work is indeed the largest term but not by much: The PW comprised 57%, 56%, 43%, and 52% of the total flux at YPO2, YPO1, CPO, and RPO respectively. The large percentage still remaining was accounted for by the advection of HKE and APE and shows that the waves were indeed strongly nonlinear. The increase in APE with respect to HKE at mooring RPO versus CPO can be accounted for by the change in the fluxes at those moorings (Figure 16a). From CPO to RPO, the kinetic energy flux dropped by 50% (blue line to green line) while the potential energy flux went up slightly (red line to purple line).

5. Summary and conclusions

An 18-day time series of high-resolution velocity and temperature data were obtained at four closely spaced moorings spanning 386-266 m depth on the continental slope 160 km northeast of Dongsha Island in the South China Sea. The experiment was motivated by the need to understand ocean variability and how it interacts with large (15 m) sand dunes on the sea floor. The dominant signal observed consisted of sets of large amplitude nonlinear internal waves (NLIWs) impinging on the continental slope from the southeast. These were in fact the very same waves that impact the Dongsha Island region and have been reported by many previous authors. The “sand dunes” waves however were about 50% smaller and less energetic than the “Dongsha” waves, since the location was near the northern extremity of the wave crests rather than near the center of the waves. The mean bottom slope along the sand dunes mooring line was also gentler than farther southwest. While the internal tides are no doubt important to the dune-building process, this paper focuses entirely on the NLIW properties, most especially how the waves were transformed as they shoaled up a very gradual bottom slope. New information gleaned includes the packet formation process, further insights on the difference between a-waves and b-waves, and the energy transformation processes which take place during wave shoaling.

During the fortnight observed, the a-waves began arriving several days ahead of the b-waves and traveled in a more northerly direction. Once they started arriving, the b-wave always lead the a-wave by 6-8 hours. In any given pair, the a-wave was generally larger, but b-waves generated near spring tide may be larger than a-waves generated near neap. The b-waves may also form packets, so that wave amplitude and packet structure are not non-ambiguous ways to classify these waves. Rather, the wave generation mechanism and their positioning relative to each other and the internal tide determines the wave classification. The wave arrival patterns rigorously track the tidal structure in Luzon Strait, even to the point of shifting by six hours when the strong beat/weak beat pattern reversed in the strait during neap tide. The b-waves were located near the head of the upslope internal tide while the a-waves developed more towards the back. The generation process is likely three-dimensional and cannot be discerned from this far-field data set. The arrival patterns were consistent with earlier work showing that the a-waves were generated in the southern portion of the Luzon Strait and the b-waves in the north.

Moved up [13]: exceptions however: wave a1 on June 3 and A7 on June 15 had much less energy arriving at RPO than was present at CPO. This may have been due to tropical storm Hagabus for the June 15 wave, but the reason is not obvious for the June 3 wave. Altogether the results are consistent with the idea of greater HKE in the larger incident waves with energy transferring from HKE to APE as the waves shoaled. The results are in reasonable agreement with theory and numerical simulations [Lamb and Nguyen, 2009; Lamb and Warn-Varnas, 2015]. ¶

Moved up [14]: ¶
In the simplest sense the energy flux is just the energy times the group velocity (or phase velocity for non-dispersive waves). Since the phase velocity varied from 1.87 m s⁻¹ between YPO2 and YPO1 to 1.69 m s⁻¹ from CPO to RPO, the flux/energy ratio is expected to vary little across the slope and the flux patterns should resemble that of the total energies. This is indeed the case as seen by comparing the envelope of the curves for the total flux (Figure 16a) and the total energy (Figure 15f). The vertically integrated flux tends to decrease upslope primarily due to the decreasing water depth. Of greater interest is the change in the various terms of equation (6). The pressure work is indeed the largest term but not by much: The PW comprised 57%, 56%, 43%, and 52% of the total flux at YPO2, YPO1, CPO, and RPO

Deleted: b

Deleted: A fortnight's worth

Deleted: and acoustic propagation

Deleted: was

Deleted: s, sometimes also called solitons

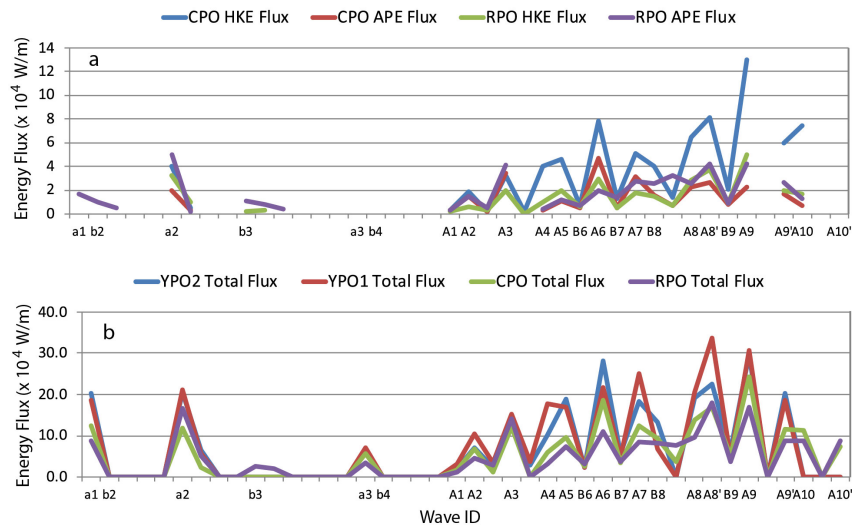
Deleted: under

Moved (insertion) [15]

Formatted: No widow/orphan control

Deleted: fortnight

Deleted: While it is tempting to ascribe the a-wave formation to the ebb tide in the strait, released when the tide turned, and the



1715
1716
1717
1718
1719
1720
1721
1722
1723
1724
1725
1726

Figure 16. The energy flux up the slope for each of the nonlinear internal waves identified in the sand dunes moored array data. a) The kinetic and potential energy flux for moorings CPO and RPO. b) The total energy flux for all four moorings. This is the sum of the kinetic, potential, and pressure work terms.

A conundrum remains the arrival of two large a-waves with nearly equal amplitude separated by two hours during the period of maximal tidal forcing, spring tide plus or minus one day. Additional work is needed to understand the origin of these waves.

1727 At least two packet-generating mechanisms were clearly observed. Most a-waves had already formed in the deep basin by the time they were incident upon the most offshore mooring, YPO2 at the 388 m isobath. The behavior of these waves depended on their amplitude: waves smaller than about 50 m and 100 MJ m⁻¹ propagated adiabatically upslope with little change of form. Waves larger/more energetic than this formed packets via wave dispersion. Wave breaking was not observed at any time, with the possible exception of the largest wave that was steepening on the backside at the shallowest mooring, RPO at 266 m depth. The waves likely break, and/or reflect, inshore of 266 m where the bottom is also steeper. On the other hand, some of the b-waves were incident on YPO2 while others were absent at YPO2 and formed while the internal tide shoaled between YPO2 and RPO. These waves and wave packets were formed by the breaking of the leading, strongly convergent edge of the upslope-propagating internal tide (not to be confused with a breaking NLIW). This process took place right at mooring CPO

Moved up [15]: During the fortnight observed, the a-waves began arriving several days ahead of the b-waves and traveled in a more northerly direction. Once they started arriving, the b-wave always lead the a-wave by 6-8 hours. In any given pair, the a-wave was generally larger, but b-waves generated near spring tide may be larger than a-waves generated near neap. The b-waves may also form packets, so that wave amplitude and packet structure are not non-ambiguous ways to classify these waves. Rather, the wave generation mechanism and their positioning relative to each other and the internal tide determines the wave classification. The wave arrival patterns rigorously track the tidal structure in Luzon Strait, even to the point of shifting by six hours when the strong beat/weak beat pattern reversed in the strait during neap tide. The b-waves were located near the head of the upslope internal tide while the a-waves developed more towards the back. While it is tempting to ascribe the a-wave formation to the ebb tide in the strait, released when the tide turned, and the

Deleted: b-waves to the previous flood, the generation process is likely three-dimensional and cannot be discerned from this far-field data set. A conundrum remains the arrival of two large a-waves with nearly

Deleted: .

1766 where a 5°C temperature front was nearly vertical. This process occurred just once
1767 per day and was most easily discerned by the downslope tidal current near the
1768 bottom which was not complicated by upper ocean processes.
1769

1770 The energy transformations also depended on wave amplitude. For the smaller
1771 waves, the incident APE was greater than the HKE and continued to grow upslope.
1772 For the larger waves, the incident HKE was larger than the APE, but the flux of HKE
1773 decreased sharply upslope especially between 342m to 266 m, while the flux of APE
1774 in that depth range increased slightly, resulting in greater APE than HKE farther
1775 onshore. These results are in rough agreement with recent theory and numerical
1776 simulations of shoaling waves.
1777

1778
1779

Deleted: Important scientific issues still remaining to be studied include the how the internal tides and waves impact the dune formation process, determining the source and generation mechanisms for the a-waves vs. the b-waves, and understanding the double a-wave phenomenon near spring tide. These topics are the subject of other works in progress. ¶

1787 **Acknowledgements**

1788

1789 This work was supported by the U.S. Office of Naval Research (ONR) under grant

1790 N000141512464 and by the Taiwan Ministry of Science and Technology (MOST).

1791 Wen-Hwa Her (IONTU) and Marla Stone (NPS) led the mooring work at sea. We

1792 thank the officers and crew of the research vessels OCEAN RESEARCHER 1, OCEAN

1793 RESEARCHER 3, and OCEAN RESEARCHER 5.

1794

1795

1796

1797

References

1798

1799 Alford, M. H., Lien, R.-C., Simmons, H., Klymak, J., Ramp, S. R., Yang, Y.-J., Tang, T.-Y.,
1800 Farmer, D., and Chang, M.-H.: Speed and evolution of nonlinear internal waves
1801 transiting the South China Sea, *J. Phys. Oceanogr.*, 40, 1338-1355, 2010.

1802

1803 Alford, M. H., MacKinnon, J. A., Nash, J. D., Simmons, H., Pickering, A., Klymak, J. M.,
1804 Pinkel, R., Sun, O., Rainville, L., Musgrave, R., Beitzel, T., Fu, K.-H., and Lu, C.-W.:
1805 Energy flux and Dissipation in Luzon Strait: Two tales of two ridges, *J. Phys.*
1806 *Oceanogr.* 41, 2211-2222, 2011.

1807

1808 Alford, M. H., Peacock, T., and co-authors: The formation and fate of internal waves
1809 in the South China Sea, *Nature*, 521, 65-69, 2015.

1810

1811 Buijsman, M. C., Kanarska, Y., and McWilliams, J. C.: On the generation and evolution
1812 of nonlinear internal waves in the South China Sea, *J. Geophys. Res.-Oceans*, 115,
1813 C02012, doi:10.1029/2009JC005275, 2010a.

1814

1815 Buijsman, M. C., McWilliams, J. C., and Jackson, C. R.: East-west asymmetry in
1816 nonlinear internal waves from Luzon Strait, *J. Geophys. Res.-Oceans*, 115, C1057,
1817 doi:10.1029/2009JC006004, 2010b.

1818

1819 [Chang, M.-H.: Marginal instability within internal solitary waves, *Geophys. Res. Lett.*, 48,](#)
1820 [e2021GL092616, <https://doi.org/10.1029/2021GL092616>, 2021.](#)

1821

1822 [Chang, M.-H., Lien, R.-C., Lamb, K. G., and Diamesis, P. J.: Long-term observations of](#)
1823 [shoaling internal solitary waves in the northern South China Sea, *J. Geophys. Res.-*](#)
1824 [Oceans, 126, <https://doi.org/10.1029/2020JC017129>, 2021.](#)

1825

1826 Chang, M.-H., Cheng, Y.-H., Yang, Y.-J., Jan, S., Ramp, S. R., Reeder, D. B., Hseih, W.-T.,
1827 Ko, D. S., Davis, K. A., Shao, H.-J., and Tseng, R.-S.: Direct measurements reveal
1828 instabilities and turbulence within large amplitude internal solitary waves beneath
1829 the ocean, *Communications Earth & Environments*, 2, doi:10.1038/S43247-020-
1830 00083-6, 2021.

1831

1832 Chen, Y.-J., Ko, D. S., and Shaw, P.-T.: The generation and propagation of internal
1833 solitary waves in the South China Sea, *J. Geophys. Res.-Oceans*, 118, 6578-6589,
1834 doi:10.1002/2013JC009319, 2013.

1835

1836 [Chiu, L. Y. S., and Reeder, D. B.: Acoustic mode coupling due to subaqueous sand](#)
1837 [dunes in the South China Sea, *J. Acoust. Soc. Am.*, 134, doi:10.1121/1.4812862, 2013.](#)
1838

Formatted: Font: 12 pt

Formatted: Font: 12 pt

Formatted: Line spacing: single, Don't adjust space between Latin and Asian text, Don't adjust space between Asian text and numbers, Tab stops: Not at 0.13"

Formatted: Font: 12 pt

Formatted: Font: 12 pt

Formatted: Font: 12 pt

Formatted: Font: 12 pt

Formatted: Font: 12 pt

Field Code Changed

Formatted: Hyperlink, Font: (Default) +Body (Cambria), 12 pt, Font color: Auto

Formatted: Font: (Default) Times New Roman, Font color: Black

Field Code Changed

Formatted: Hyperlink, Font: Times, 12 pt, Font color: Auto

1839 [Chiu, L. Y. S., Chang, A. Y. Y., and Reeder, D. B.: Resonant interaction of acoustic](#)
1840 [waves with subaqueous bedforms: Sand dunes in the South China Sea, J. Acoust. Soc.](#)
1841 [Am., 138, doi:10.1121/1.4937746, 2015.](#)
1842
1843 Du, T., Tseng, Y.-H., and Yan, X.-H.: Impacts of tidal currents and Kuroshio intrusion
1844 on the generation of nonlinear internal waves in Luzon Strait, J. Geophys. Res.-
1845 Oceans, 113, C08015, doi:10.1029/2007JC004294, 2008.
1846
1847 Duda, T. F., Lynch, J. F., Irish, J. D., Beardsley, R. C., Ramp, S. R., Chiu, C.-S., Tang,
1848 T.-Y., and Yang, Y.-J.: Internal tide and nonlinear internal wave behavior at the
1849 continental slope in the northern South China Sea, IEEE/J. Oc. Eng., 29, 1105-
1850 1131, 2004.
1851
1852 [Egbert, G., and Erofeeva, S.: Efficient inverse modeling of barotropic ocean tides,](#)
1853 [J. Atmos. Oceanic Technol., 19, 183-204, 2002.](#)
1854
1855 Farmer, D., Li, Q., and Park, J.-H.: Internal wave observations in the South China Sea:
1856 The role of rotation and non-linearity, Atmosphere-Ocean, 47, 267-280, 2009.
1857
1858 Grimshaw, R., Guo, C., Helfrich, K., and Vlasenko, V.: Combined effect of rotation and
1859 topography on shoaling oceanic internal solitary waves, J. Phys. Oceanogr., 44, 1116-
1860 1132, 2014.
1861
1862 Jackson, C. B.: An empirical model for estimating the geographic location of
1863 nonlinear internal solitary waves, J. Atmos. Oceanic Technol., 26, 2243-2255, 2009.
1864
1865 Klymak, J. M., Pinkel, R., Liu, C.-T., Liu, A. K., and David, L.: Prototypical solitons in
1866 the South China Sea, Geophys. Res. Lett., 33, L11607,
1867 doi:10.1029/2006GL025932, 2006.
1868
1869 Kunze, E., Rosenfeld, L. K., Carter, G. S, and Gregg, M. C.: Internal waves in
1870 Monterey Submarine Canyon, J. Phys. Oceanogr., 32, 1890-1913, 2002.
1871
1872 [Helfrich, K. R., Trowbridge, J. H., and Reeder, D. B.: High dissipation of an internal](#)
1873 [solitary wave over sand dunes, J. Phys. Oceanogr., in review.](#)
1874
1875 Lamb, K. G.: A numerical investigation of solitary internal waves with trapped
1876 cores formed via shoaling, J. Fluid Mech., 451, 109-144, 2002.
1877
1878 Lamb, K. G., and Nguyen, V. T.: Calculating energy flux in internal solitary waves with
1879 an application to reflectance, J. Phys. Oceanogr., 39, 559-580, 2009.
1880

Deleted: ¶

1882 Lamb, K. G., and Warn-Varnas, A.: Two-dimensional numerical simulations of
 1883 shoaling internal solitary waves at the ASIAEX site in the South China Sea, *Nonlin.*
 1884 *Processes Geophys.*, 22, 289-312, 2015.

1885
 1886 Lee, C. M, Kunze, E., Sanford, T. B., Nash, J. D., Merrifield, M. A., and Holloway, P.
 1887 E.: Internal tides and turbulence along the 3000-m isobath of the Hawaiian
 1888 Ridge, *J. Phys. Oceanogr.*, 36, 1165-1183, 2006.

1889
 1890 Li, Q., and Farmer, D. M.: The generation and evolution of nonlinear internal
 1891 waves in the deep basin of the South China Sea, *J. Phys. Oceanogr.*, 41, 1345-
 1892 1363, 2011.

1893
 1894 Lien, R. C., D'Asaro, E. A., Henyey, F., Chang, M. H., Tang, T. Y. and Yang, Y.-J.:
 1895 Trapped core formation within a shoaling nonlinear internal wave, *J. Phys.*
 1896 *Oceanogr.*, 42, 511-525 2012.

1897
 1898 Lien, R. C., Henyey, F., Ma, B., and Yang, Y. J.: Large-amplitude internal solitary
 1899 waves observed in the northern South China Sea: Properties and Energetics, *J.*
 1900 *Phys. Oceanogr.*, 44, 1095-1115, 2014.

1901
 1902 Liu, A. K., Ramp, S. R., Zhao, Y., and Tang, T. Y.: A case study of internal solitary wave
 1903 propagation during ASIAEX 2001, *IEEE/J. Oc. Eng.*, 29, 1144-1156, 2004.

1904
 1905 Moum, J. N., Klymak, J. M., Nash, J. D., Perlin, A., and Smyth, W. D.: Energy
 1906 transport by nonlinear internal waves, *J. Phys. Oceanogr.*, 37, 1968-1988, 2007.

1907
 1908 Nash, J. D., Alford, M. H., and Kunze, E.: Estimating internal wave energy fluxes in the
 1909 ocean, *J. Atm. and Oc. Tech.*, 22, 1551-1570, 2005.

1910
 1911 Nash, J. D., Kunze, E., Lee, C. M., and Sanford, T. B.: Structure of the baroclinic tide
 1912 generated at Kaena Ridge, Hawaii, *J. Phys. Oceanogr.*, 36, 1123-1135, 2006.

1913
 1914 Nash, J. D., Kelly, S. M., Shroyer, E. L., Moum, J. N., and Duda, T. F.: The unpredictable
 1915 nature of internal tides on the continental shelf, *J. Phys. Oceanogr.*, 42, 1981-2000,
 1916 2012.

1917
 1918 Orr, M. H., Mignerey, P. C.: Nonlinear internal waves in the South China Sea:
 1919 Observations of the conversion of depression internal waves to elevation internal
 1920 wages, *J. Geophys. Res.* 108, 3064, doi:10.1029/2001JC001163, 2003.

1921
 1922 Ramp, S.R., Chiu, C. S., Kim, H.-R., Bahr, F. L., Tang, T.-Y., Yang, Y. J., Duda, T., and
 1923 Liu, A. K.: Solitons in the Northeastern South China Sea Part I: Sources and
 1924 Propagation Through Deep Water, *IEEE/J. Oc. Eng.*, 29, 1157-1181, 2004.

Deleted: ¶



1927
1928 Ramp, S. R., Yang, Y. J., and Bahr, F. L.: Characterizing the nonlinear internal wave
1929 climate in the northeastern South China Sea, *Nonlin. Processes Geophys.*, 17, 481-
1930 498, doi:10.5194/npg-17-481-2010, 2010.
1931
1932 Ramp, S. R., Park, J.-H., Yang, Y. J., Bahr, F. L., and Jeon, C.: Latitudinal Structure of
1933 Solitons in the South China Sea, *J. Phys. Oceanogr.*, 49, 1747-1767, 2019.
1934
1935 Ramp, S. R., Yang, Y.-J., Jan, S., Chang, M.-H., Davis, K. A., Sinnett, G., Bahr, F. L.,
1936 Reeder, D. B., Ko, D. S., and Pawlak, G.: Solitary waves impinging on an isolated
1937 tropical reef: Arrival patterns and wave transformation under shoaling, *J. Geophys. Res.-*
1938 Oceans, in review.
1939
1940 Reeder, D. B., Ma, B., and Yang, Y. J.: Very large subaqueous sand dunes on the upper
1941 continental slope in the South China Sea generated by episodic, shoaling deep-water
1942 internal solitary waves, *Mar. Geol.*, 279, 12-18, 2011.
1943
1944 Rivera-Rosario, G., Diamessis, P. J., Lien, R.-C., Lamb, K. G., & Thomsen, G. N.:
1945 Formation of recirculating cores in convectively breaking internal solitary waves of
1946 depression shoaling over gentle slopes in the South China Sea, *J. Phys. Oceanogr.*, 50,
1947 1137–1157, <https://doi.org/10.1175/jpo-d-19-0036.1>, 2020.
1948
1949 Scotti, A., Beardsley, R. C., and Butman, B.: On the interpretation of energy and
1950 energy fluxes of nonlinear internal waves: An example from Massachusetts Bay, *J.*
1951 *Fluid Mech.*, 561, 103-112, 2006.
1952
1953 Small, J.: A nonlinear model of the shoaling and refraction of interfacial solitary
1954 waves in the ocean. Part I: Development of the model and investigations of the
1955 shoaling effect, *J. Phys. Oceanogr.*, 31, 3163-3183, 2001.
1956
1957 Small, J.: A nonlinear model of the shoaling and refraction of interfacial solitary
1958 waves in the ocean. Part II: Oblique refraction across a continental slope and
1959 propagation over a seamount, *J. Phys. Oceanogr.*, 31, 3184-3199, 2001.
1960
1961 Turkington, B., Eydeland, A., and Wang, S.: A computational method for solitary
1962 internal waves in a continuously stratified fluid, *Stud. Appl. Maths.*, 85, 93-127,
1963 1991.
1964
1965 Vlasenko, V., Ostrovsky, V. L., and Hutter, K.: Adiabatic behavior of strongly
1966 nonlinear internal solitary waves in slope-shelf areas, *J. Geophys. Res.*, 110, C04006,
1967 doi:10.1029/2004JC002705, 2005.
1968
1969 Vlasenko, V., Guo, C., and Stashchuk, N.: On the mechanism of A-type and B-type
1970 internal solitary wave generation in the northern South China Sea, *Deep-Sea Res. I*,
1971 69, 100-112, 2012.
1972

Deleted: 0

Formatted: Font: Times New Roman, 12 pt

Formatted: Font: Times New Roman, 12 pt

Formatted: Font: Times New Roman, 12 pt, Not Italic

Formatted: Font: Not Italic

Formatted: Font: Times New Roman, 12 pt, Not Italic

Formatted: Font: Not Italic

Formatted: Font: Times New Roman, 12 pt, Not Italic

Formatted: Font: Not Italic

Formatted: Font: Times New Roman, 12 pt

Field Code Changed

Formatted: Hyperlink, Font: (Default) Times New Roman, 12 pt, Font color: Auto

Deleted: ¶

Formatted: Font: (Default) Times New Roman

1975 Vlasenko, V., and Stashchuk, N.: Three-dimensional shoaling of large-amplitude
1976 internal waves, *J. Geophys. Res.-Oceans*, 112, C11018, doi:10.1029/2007JC004107,
1977 2007.
1978
1979 Vlasenko, V., and Hutter, K.: Numerical experiments on the breaking of solitary
1980 internal waves over a slope-shelf topography, *J. Phys. Oceanogr.*, 32, 1779-1793,
1981 2002.
1982
1983 Yang, Y. J., Fang, Y. C., Chang, M.-H., Ramp, S. R., Kao, C.-C., and Tang, T.-Y.:
1984 Observations of second baroclinic mode internal solitary waves on the continental
1985 slope of the northern South China Sea, *J. Geophys. Res.-Oceans*, 114, C10003,
1986 doi:10.1029/2009JC005318, 2009.
1987
1988 Yang, Y. J., Fang, Y. C., Chang, Y.-T., Tang, T. Y., and Ramp, S. R.: Convex and concave
1989 types of second baroclinic mode internal solitary waves, *Nonlin. Processes*
1990 *Geophys.*, 17, 605-614, doi:10.5194/npg-17-605-2010, 2010.
1991
1992 Zhang, Z., Fringer, O. B., and Ramp, S. R.: Three-dimensional, nonhydrostatic
1993 numerical simulation of nonlinear internal wave generation and propagation in the
1994 South China Sea, *J. Geophys. Res.-Oceans*, 116, C05022, doi:10.1029/2010JC006424,
1995 2011.
1996
1997
1998
1999
2000
2001
2002

2003
2004

APPENDIX A

Table 1. Mooring and Instrument Locations and Performance

Mooring	Latitude (north)	Longitude (east)	Bottom Depth (m)	Instrument	Instrument Depth (m)	Start	Stop	Record Length (d)	Sample Interval (s)	Number of Points
RPO	21 53.334	117 33.676	266			6/1/14	6/18/14	18		
				★ADCP 300 kHz	31				90	17198
				★ADCP 300 kHz	105				90	17197
				★ADCP 300 kHz	190				90	17198
				SBE 37 (TSP)	27, 105, 184, 244			20	76354	
				SBE 39 (TP)	61, 91, 141, 170, 258			10	154792	
				SPE 56 (T)	45, 75, 125, 155, 199, 229			10	154794	
CPO	21 51.879	117 36.587	342			6/1/14	6/18/14	18		
				★ADCP 300 kHz	11				90	16394
				◆ADCP 300 kHz	263				90	16398
				★ADCP 300 kHz	269				90	16410
				SBE 37 (TSP)	43, 109, 169, 230, 307			10	148066	
				SBE 39 (TP)	78, 139, 200, 286			10	148066	
YPO1	21 49.998	117 37.600	372			6/2/14	6/19/14	18		
				♣ADCP 75 kHz	20				90	16537
				★ADCP 300 kHz	306				90	16537
				SBE 19 (TSP)	369		6/13/14	12	15	63517
				SBE 39 (TP)	35, 56, 92, 117, 178, 240				10	148845
				SBE 39 (TP)	300		6/17/14	16	10	134727
				SBE 39 (TP)	354		6/10/14	9	10	70620
				SBE 56 (T)	76		6/8/14	7	10	54078
				SBE 56 (T)	147, 209, 270, 325				10	148845
				Star Oddi (TP)	148, 188		6/11/14	10	10	77398
YPO2	21 48.679	117 39.512	386			6/2/14	6/19/14	18		
				♣ADCP 75 kHz	20				90	16916
				★ADCP 300 kHz	301				90	16915
				SBE 39 (TP)	58, 97, 118, 180, 241				10	152252
				SBE 39 (TP)	37, 354		6/17/14		10	133147
SBE 56 (T)	78, 149, 201, 272, 328				10	152252				
Source	21 52.630	117 37.128	328			6/1/14	6/18/14	18		
				SBE 37 (TSP)	26, 86, 147, 208, 268				10	142186
				SBE 39 (TP)	55, 116, 174, 238, 310				10	1142186
★4-m bins down-looking, 30 pings per ensemble ◆4-m bins up-looking, 30 pings per ensemble ♣16-m bins down-looking, 10 pings per ensemble										

Field Code Changed

2005

Page 9: [1] Deleted	Steven Ramp	1/20/22 12:54:00 PM
Page 11: [2] Deleted	Steven Ramp	1/24/22 10:40:00 AM
Page 11: [3] Deleted	Steven Ramp	1/24/22 11:00:00 AM
Page 11: [4] Deleted	Steven Ramp	1/24/22 11:50:00 AM
Page 19: [5] Deleted	Steven Ramp	1/31/22 1:07:00 PM
Page 24: [6] Deleted	Steven Ramp	1/31/22 1:40:00 PM